

K-Band Land-Mobile Satellite Channel Characterization Using ACTS

Michael Rice*, Deborah S. Pinck†, Jeffrey Slack, Brian Humpherys

Summary

K-band pilot tone data collected by the ACTS Mobile Terminal (AMT) during 1994 are used to characterize the K-band land-mobile satellite channel. The characterization is two-fold: a probability density model is derived which shows that the fade exceedance levels at K-band are much higher than those at lower frequencies, particularly at L-band. Further, the fade statistics are very dependent on the geometry of the surrounding environment. The difference between good and bad environments is much more pronounced at K-band than at L-band. A discrete time model is used to provide insight into the bursty nature of the errors induced by propagation effects on the channel. For a data rate of 9600 bits/sec, the average fade duration for a fade threshold of 6 dB is on the order of a few thousand bits which corresponds to a fade duration of 2 to 5 meters. The fade durations are typical of those at L-band which suggests that while the K-band fades are more severe than those at L-band, the durations are approximately the same.

1 Introduction

Land mobile satellite systems allow truly ubiquitous wireless communications to users almost anywhere at anytime. Mobile satellite systems are better suited to providing voice and data communications services to users traveling in low population density areas while land based cellular systems are better suited to providing these services in high population density areas. As the increasing demand for mobile communication capacity consumes the available bandwidth allocations at L-, S-, and Ku-bands, K- and Ka-band frequencies offer potential relief.

The communication channel between a satellite and a land based mobile user presents a challenge. Multipath interference and shadowing cause severe variations in the received

*M. Rice, J. Slack, and B. Humpherys are with the Department of Electrical & Computer Engineering, Brigham Young University, Provo, UT 84602.

†D. Pinck is with the Jet Propulsion Laboratory, California Institute of Technology, Mail Stop 161-241, 4800 Oak Grove Drive, Pasadena, CA 91109.

power making constant, reliable communications difficult and limiting system performance. The effects of shadowing are the most severe source of signal outages in a land mobile satellite system. The attenuation due to shadowing increases with frequency: L-band is worse than UHF, S-band is worse than L-band, etc. Since K-band frequencies are ten times those at L-band, a thorough and careful analysis of the fading effects is required to assess the viability of K-band mobile satellite systems.

NASA's Advanced Communications Technology Satellite (ACTS) provides an ideal space-based platform for analyzing the K-band mobile satellite channel. This paper reports on the results of the K-band mobile propagation analysis campaign using the ACTS Mobile Terminal (AMT) developed by the Jet Propulsion Laboratory (JPL). The channel is modeled in two ways:

- A probability density model is derived from frequency histograms of measured data. This model allows designers to predict 1 %, 5%, and 10% fade exceedance levels.
- A discrete time fade duration model is developed which provides information regarding the burst error nature of the channel, the average fade durations, and signal outage percentages.

The system used to collect the data and a description of the environment are outlined in Section 2. The probability density model is described in Section 3 and the discrete time model in Section 4.

2 Experiment Description

NASA's ACTS satellite provides a stationary platform ideally suited to the measurement of mobile propagation effects at K/Ka-band (20/30 GHz). JPL has developed a proof-of-concept breadboard mobile terminal system to operate in conjunction with ACTS at K/Ka-band called the ACTS Mobile Terminal (AMT) [1]. Field tests conducted during the first 7 months of 1994 using JPL's AMT provide channel characterization data for the K-band land-mobile satellite channel.

As depicted in Figure 1, the system is comprised of a bent pipe propagation link connecting terminals at fixed and mobile sites. The forward channel originated at the fixed station with a 29.634 GHz pilot tone. This pilot tone was received by ACTS, mixed to the downlink frequency of 19.914 GHz, and transmitted on the Southern California spot beam. The forward channel offered a composite C/N_0 of 55.63 dB-Hz and was the basis for the K-band results.

The AMT is equipped with a small (8" x 3") high-gain reflector antenna [2] which tracks the satellite in azimuth for a fixed elevation angle (46° for these experiments). The antenna is mechanically steered and acquires and tracks the satellite over the entire 360° of azimuth with a pointing error less than 2°. Vehicle turn rates of up to 44° per second can be accommodated. The antenna has a G/T of -6 dB/K over a band width of 300 MHz. The 3 dB beam width

is $\pm 9^\circ$ in elevation and $\pm 6^\circ$ in azimuth. The antenna pointing system enables the antenna to track the satellite for all practical vehicle maneuvers.

The Data Acquisition System (DAS) illustrated in Figure 2 measures in-phase pilot voltage level and the non-coherent pilot power level. The in-phase pilot voltage level was sampled at 4000 samples/second in a bandwidth of 1.5 kHz and was used to analyze the channel characteristics presented in this paper. The data were stored on 5 Gbyte Exabyte tapes for off-line evaluation. The vehicle position, vehicle velocity, and time stamp were derived from an on-board GPS system and updated once each second. The DAS also provides real-time displays of various parameters to aid the experimenters in the field.

Data were collected in a variety of locations in order to characterize environments typical of mobile satellite applications. In the absence of any standard definitions for the various environmental conditions typical of land mobile satellite channels, a set of general classifications specific to Southern California was adopted. A 11 runs in this measurement campaign were conducted in Pasadena, California which presents a seasonally invariant suburban environment. The environments are divided into three broad categories based on the type of road way:

Category I: a limited access multi-lane freeway

Category II: a broad suburban thoroughfare lined with trees and buildings. The tree canopies cause intermittent blockage and the buildings are either too far removed from the road side or not tall enough to cause significant blockage.

Category III: a small, two-lane roadway lined with trees and buildings. The tree canopies often cover the entire road way and buildings are close enough to contribute to the fading process.

This description is most appropriate in this case since the type and kind of obstructions are strongly dependent on the nature of the road. Table 1 shows a summary of the environmental features of the AMT runs.

3 Probability Density Model

3.1 Theoretical Considerations

The primary contributors to signal fluctuations in the land-mobile satellite channel are multipath interference and shadowing [3]. Multipath interference is the destructive interference caused by the reception of randomly phased reflections of the transmitted signal [4]. The transmitted satellite signal received by the mobile terminal consists of three major components:

1. The Line-Of-Sight (LOS) Component which arrives at the receiver via a direct path

2. The Specular Component which consists of a small number of reflections. Typically, the dominant reflection is the ground reflection which arrives at the receiver at a negative elevation angle and can be neglected due to the attenuation effects of the upward-looking receiver antenna [5].
3. The Diffuse Component which consists of a large number of weak reflections with random amplitudes and phases.

As shown in Appendix A, the resulting fluctuations in received power S are described statistically by the non-central chi-square distribution parameterized by the ratio κ of direct (LOS) to diffuse signal power:

$$p(S; \kappa) = \kappa e^{-\kappa(1+S)} I_0(2\kappa\sqrt{S}) \quad (1)$$

In the event the LOS component is completely blocked, $\kappa = 0$ and the fluctuations in received power are described statistically by the non-central chi-square distribution² [6]

$$p(S; \mathbf{0}) = \frac{1}{S_0} \exp\left(-\frac{S}{S_0}\right) \quad (2)$$

where S_0 is the mean received signal power.

Shadowing is the complete or partial obstruction of the transmitted signal caused by the absorption and scattering of the incident direct signal by roadside trees or other obstacles in the path between the satellite and the vehicle [3]. Mobile satellite experiments at L-band [7, 8] show that the effects of shadowing dominate the statistics of the received signal. Terrestrial measurements at UHF [9, 10, 11] and X-band [12] show that the shadowing process is approximated by the log-normal distribution. Loo [13] and Lutz [14] have used the log-normal distribution to successfully model the signal attenuation due to shadowing for the land-mobile satellite channel. In this case, the statistics of the resulting variations in the mean received signal power S_0 follow

$$f(S_0) = \frac{10}{\sqrt{2\pi\sigma \ln 10}} \frac{1}{S_0} \exp\left[-\frac{(10 \log S_0 - \mu)^2}{2\sigma^2}\right] \quad (3)$$

where μ is the mean power level decrease in dB and σ^2 is the variance of the power level due to shadowing.

The combination of multipath interference and shadowing manifests itself as relatively rapid variations about a local mean signal power (due to the multipath interference) superimposed on relatively slow variations in the received signal power (due to shadowing) [15]. The superposition of the two processes is modeled by conditioning one of the pdf's (1) or (2)

¹Such channels are usually referred to as "Ricean" since the envelope of the received signal follows the Rice distribution.

²This case is usually referred to as a Rayleigh channel since the envelope of the received signal follows the Rayleigh distribution.

on the mean received signal power S_0 and using the log-normal pdf (3) for S_0 [15, 16, 17, 13]. Lutz, et. al. extended this approach in a novel way by introducing a “time share” between shadowed and unshadowed fading [14] to model the L-band mobile satellite data collected in Europe. Under this formulation, the received signal power follows the non-central chi-square distribution for the unshadowed fading scenario and the central chi-square/log-normal distribution for shadowed fading. The parameter S_0 in (2) serves as the conditional variable so that the pdf of the received signal power is

$$p(S) = Ap(S; \kappa) + (1 - A) \int_0^\infty p(S; 0) f(S_0) dS_0 \quad (4)$$

where the time share parameter $0 < A < 1$ represents the proportion of total distance (or time) the received signal is shadowed. The notion of time share was also observed by Goldhirsh and Vogel [18] in examining K-band mobile satellite data and has also been successfully applied to the analysis of mobile satellite channels by Castro [19] and Vucetic [20].

Other factors contributing to variations in the received signal power include thermal noise, Faraday rotation, and ionospheric scintillation [20]. The contribution of these factors relative to the fading caused by shadowing and multipath interference is so small that these effects may be ignored on a well designed satellite link.

3.2 Description of Measured Data

Time series for two representative runs are illustrated in Figures 3 and 4. In these plots, the received pilot power is normalized to the power of unshadowed line-of-sight power level. These plots show characteristics typical of land mobile satellite communication systems: shallow fades due to multipath interference and deep fades due to shadowing superimposed on slow variations in the mean signal power due to changes in the shadowing profile of the local environment.

The cumulative fade distributions for several representative runs are shown in Figure 5. All curves have a distinct characteristic: a “knee” at 2 to 3 dB signifying a transition region between fading due to multipath interference and fading due to shadowing. The curve is steep for the first few dB which is typical of Ricean fading. Below the transition region, the curve exhibits a more gradual roll-off characteristic of an exponential dependency. These plots show clearly the time share nature of the fading processes at K-band. This characteristic shape has also been observed at L-band [14, 21, 8], at S- and Ku-bands [21], and at K-band [18]. The 1%, 5%, and 10% fade exceedance levels are typically used to describe the shape of the histogram and are tabulated for all runs of the AMT campaign in Table 2.

The results of the sole category I run were expected. The absence of obstructions combined with the rejection of any off-axis reflections by the narrow-beam antenna produced a signal with little appreciable multipath interference.

The results of the category II runs are mixed. For the north-south runs where the lane tree geometry provided a relatively clear path to the satellite, the results are promising; 1 %

fade levels range from 8 to 10 dB while the 10% fade levels are all about 1 dB. The other north-south runs were conducted on lanes too close to the trees for an unobstructed path to the satellite to be continuously available. These runs display severe fading with 1 % fade levels 27 dB or greater and 10% fade levels varying from 7.5 to 30 dB. For example, runs 072409- 072412 were all conducted in different lanes of Orange Grove 1 Blvd. The western most lane (run 072409- the south bound right lane) provides the best view to the satellite resulting in the lowest fade exceedance levels of the four runs. The fade exceedance levels become progressively worse as the run lane move west culminating in run 072410 (north bound right lane). The difference in 1070 fade exceedance levels between the “best” and “worst” lanes here is 25.5 dB. The channel characteristics are extremely sensitive to lane changes.

All the east-west runs (runs 072405- 072408) show deep fades at the 1 % level but very moderate fades at the 5% and 10% levels. This characteristic is to be expected since the azimuth to the satellite is 150° (S SE) so that routes with a roughly north-south direction may find unobstructed “seams” between the foliage lining the road. Thus the east-west runs are as good as the best north-south runs 90% to 95% of the time but are much worse 1 %. Of the times since the line-of-sight path is always skirting the tops of the trees. Runs 071016 and 071017 were particularly interesting in that the routes had isolated locations where the trees produced severe shadowing but were relatively clear in all other areas. This characteristic is reflected in the low 5% and 10% fade exceedance levels (~ 2 dB) together with very high 1 % fade exceedance levels (~ 25 dB).

With one exception, all category III runs showed deep fades well in excess of 30 dB at the 1% level and ranging from 27 to 30 dB at the 10% level. The lone exception was Run 070906” where the orientation between that particular lane and the trees lining the road allowed an unobstructed view of the satellite for most of the run the same characteristic observed in the category II runs. The inability of the K band signal to penetrate the foliage together with the rejection of off-axis reflections by the narrow-beam antenna severely limit the received satellite signal.

The 1%, 5%, and 10% fade exceedance levels are helpful in facilitating comparisons with other measurement campaigns in different locations and at different frequencies. As pointed out in [21] the absence of standard definitions for various environmental categories makes the reporting of the results and comparison of the results with other measurement campaigns problematic even when the environments for different experiments are classified in the same general categories. However, some general conclusions may be drawn from the data. Tables 3 to 6 summarize the most similar conditions from other land-mobile experiments reported.

The 1,-band experiments reported in [8] show that for constant environment, the fade exceedance levels increase as the antenna beam pattern narrows while the experiments reported in [21] show that, for constant environment, the fade exceedance levels increase as frequency increases. Thus, as expected, the fade exceedance levels for the narrow-beam, K-band AMT experiments show deeper 1 % percent fade exceedance levels than the corresponding 1,-band experiments. While the 1%, fade exceedance levels for the AMT experiments are greater, most of the 10% levels are 10WC1. This shows that the time-share characteristic of the fading

process is much more pronounced for the AMT experiments. The increased effect is due to the combination of the narrow beam antenna and the severe shadowing caused by foliage at K-band.

The AMT results are quite similar to the K-band results reported in [18] which are summarized in Table 6. The differences are small and are due primarily to the different environments. Compared to the experiments conducted in Texas, the AMT experiments were performed using a receive antenna with a narrower beam-width at a lower elevation angle. This combination produced slightly deeper fade exceedance levels for what appear to be roughly similar environments.

The time share characteristic of the cumulative fade distributions suggests application of the model derived by Lutz to this data. Figure 6 shows least square curve fit of (4) to run 072406. Note that there is general agreement between the two curves reinforcing the time share nature of the fading processes. However, the curves do not agree well in the transition region. This effect is due primarily to antenna effects as follows.

The azimuth plane of the fixed-elevation AMT antenna experiences the same pitch and roll as the vehicle which, on typical road surfaces, leads to pointing errors as high as 4° in elevation and 3° in azimuth [22]. When coupled with the narrow-beam antenna, these pointing errors cause degradations in the line-of-sight signal level by as much as 2 dB [22]. The variations in the line-of-sight signal level affect the steep portion of the histogram, especially in the transition region (which is about 2 dB below the unobstructed line-of-sight level). The result is a significant difference in the transition region between the histogram and the model which assumes a constant line-of-sight signal level.

The results of the curve fitting for all runs conducted during the AMT propagation campaign are summarized in Table 2. Several of the model curves are marginal approximations due to the severe effects outlined in the previous paragraph. For most of the runs, $\kappa \sim 20$ dB which shows that when an unobstructed line-of-sight signal is available, the channel is quite good. This result is consistent with results predicted in [23] for a narrow beam antenna. The summary shows that the values of the time share parameter A are quite poor for category 111 runs and are varied for the category 1 I runs. Lutz [14] suggests that, this value indicates the amount of time the channel is available for reliable communication. However, fade duration statistics are needed to accurately predict this value. The fade duration statistics are derived from the discrete channel.

4 Discrete Channel Model

4.1 Theoretical Considerations

The probability density models do not provide a convenient method for generating representative time-series simulations of the fading events. Digital channel models, on the other hand, describe the bit error patterns at the channel output and are useful for simulating the error bursts which occur on real channels.

The land-mobile satellite channel belongs to a class of channels which possess "memory"

[24]. On such channels, the errors occur in clusters separated by fairly long error free gaps. Digital models which simulate the channel transitions from “good” to “bad” have been proposed [24] -[31]. These models attempt to generate error sequences statistically consistent with those appearing on the actual channel. The model considered here is the two-state Markov chain illustrated in Figure 7 first proposed by Gilbert [32] to model the error bursts on telephone lines. This model is suitable since it exploits the observation that, due to shadowing in typical land-mobile satellite applications, the received signal power is either high enough to permit reliable communications or so low that signal acquisition is lost. The Gilbert model attempts to recreate the dual nature of the bit error processes observed on a channel with memory. Channel state 0 is an ideal error-free channel which models the time when the channel state is “good” and no channel errors occur. Channel state 1 is a binary symmetric channel with a transition probability of 1/2 which models the time when the channel state is “bad” and error bursts occur. States 0 and 1 correspond to non-fade events and fade events, respectively.

The state transitions are described by the state transition probabilities which are usually given by the “state transition matrix”

$$\mathbf{P} = \begin{bmatrix} p_{00} & p_{01} \\ p_{10} & p_{11} \end{bmatrix} \quad (5)$$

where p_{ij} is the probability of a transition from state i to state j . Since the Markov chain model is ergodic [33] there is an associated “long run distribution”

$$\boldsymbol{\pi} = [\pi_0 \pi_1] \quad (6)$$

where π_i is the proportion of the total time that the process is in state i after a “long time.” For the special case of the two state Markov chain, the elements of $\boldsymbol{\pi}$ are given by [33]

$$\pi_0 = \frac{p_{10}}{p_{01} + p_{10}} = \frac{\overline{D}_1}{\overline{D}_0 + \overline{D}_1} \quad (7)$$

$$\pi_1 = \frac{p_{01}}{p_{01} + p_{10}} = \frac{\overline{D}_0}{\overline{D}_0 + \overline{D}_1} \quad (8)$$

where \overline{D}_i is the mean dwell time in state i and is given by [33]

$$\overline{D}_i = \frac{1}{1 - p_{ii}} \quad (9)$$

The Gilbert model can be used to determine the statistics of the fade and non-fade durations. When measured in distance (meters) the fade and non-fade duration are denoted $D_F(m)$ and $D_N(m)$, respectively. When measured in bits, they are denoted $D_F(b)$ and $D_N(b)$. The state transition probabilities p_{00} and p_{11} are on a bit by bit basis so that the probability $D_N(b)$ or $D_F(b)$ exceeds n bits is equivalent to the probability that the Markov

chain dwells in state 0 or 1 longer than “2 “steps.” These probabilities are well known and are given by [33]

$$\Pr \{ D_N(b) > n \} = p_{00}^n \quad (10)$$

$$\Pr \{ D_F(b) > n+1 \} = p_{11}^n. \quad (11)$$

The average non-fade and fade durations measured in bits ($\overline{D_N(b)}$ and $\overline{D_F(b)}$, respectively) are the mean dwell times in states 0 and 1 which are given by Equation (9).

For a given sampling interval T_s , vehicle velocity v , and transmitted bit rate R_b , each sample represents pilot tone power data through T_s seconds, vT_s meters, or R_bT_s bits. Thus $D_N(b)$ and $D_F(b)$ are related to $D_N(m)$ and $D_F(m)$ by

$$D_N(m) = \frac{v}{R_b} D_N(b) \quad (12)$$

$$D_F(m) = \frac{v}{R_b} D_F(b). \quad (13)$$

Note that using this model, $D_N(m)$ has an exponential density which is consistent with the results of [7, 19, 34]. The Gilbert model also generates an exponential density for $D_F(m)$ which is inconsistent with the Gaussian behavior postulated by Rice [35] and the log-normal behavior observed by Hase, Vogel, and Goldhirsh [7]. The Rice result describes the fade duration due to multipath interference. The duration of these fades is quite short compared to the duration of fades generated by the shadowing process. The log-normal distribution is a good model for the duration of fades of moderate depth and length [7]. Experimental results at 1.5-band indicate that the durations of longer, deeper fades are well approximated by the exponential distribution [14] produced by the Gilbert model. In the AMT experiments, shadowing is by far the most dominant cause of fades—especially those with longer durations. Thus it is expected that the fades of relatively long duration follow the exponential distribution while those of shorter duration do not. This characteristic was observed in the measured data and will be discussed in Section 4.2.

4.2 Description of Measured Data

Histograms of the distributions of $D_N(b)$ and $D_F(b)$ ³ derived from measured pilot tone data were plotted on a log scale (where the exponential distribution is a straight line). To determine suitable values of state transition matrix \mathbf{P} , a least-squares straight-line fit to that portion of the data representing long fade durations defines the best fit of the data to the exponential distribution. The slope of the line determines the value for p_{00} or p_{11} (see Equation (10) or (11), respectively).

Figures 8 and 9 show histograms of the distributions for $D_N(b)$ and $D_F(b)$ derived from the measured pilot tone data for a representative run using $L = 6$ dB and $R_b = 9600$ bps

³A fade occurs when the received pilot power level falls below a threshold which is L dB below the line-of-sight power reference level. Two cases were considered in the data analysis. The first used $L = 6$ dB which is the link margin available on the AMT experiments while the second case used $L = 10$ dB.

for $v = 48$ km/hr. For this data set, $\pi_1 = 0.049$. The plots also include the straight line approximation which represents the best fit of the data to the exponential distribution. The resulting values are $p_{00} = 1 - 5 \times 10^{-6}$ and $p_{11} = 1 - 6.95 \times 10^{-4}$.

For small values of n , the histogram does not follow the straight, line approximation. This is due to the fact that the fading process is a mixture of multipath interference and shadowing. Short fades are due primarily to multipath interference which is described more accurately by the normal distribution postulated by Rice [35] and outlined above. The fades of medium duration seem to follow the log-normal distribution [7] while the longer fades due solely to shadowing are approximated by the exponential distribution. The Gilbert model thus provides a nice first order approximation for the statistics of the fade durations due to shadowing which is the primary contributor to signal degradation in the land-mobile satellite environment. Fades due to multipath fading may be incorporated into the digital model by enlarging the number of states and assigning suitable transition probabilities [25]-[31]. It should be noted, however, that as the models represent the channel conditions more and more accurately, the complexity tends to an analytically unwieldy model which neutralizes any advantage gained from considering the model in the first place.

The parameters of the Gilbert model for the AMT runs are summarized in Tables 8 and 9. For a bit rate of 9600 bits/sec and a fade threshold of $L = 6$ dB, average fade durations for category II runs range from a few hundred to a few thousand bits while for typical category III runs, the average fade durations last 3000 to 8000 bits.

The parameter π_1 provides an estimate of the proportion of the total time (or distance) the run experienced a fade. For a fade threshold of $L = 6$ dB, the best, category I runs show 1% to 5% signal outages while the bad category II runs show 22% to 49% signal outages. A typical category III run shows 33% to 52% signal outage. If the fade threshold is dropped to $L = 10$ dB, then the best signal outages for the best category II runs range from less than 1% to about 3% while the signal outages for typical category III runs drop below 50%. As expected, link margin may be exchanged for increased signal availability.

There is only a weak correlation between the signal outage (π_1) and the average fade duration \bar{D}_F . In general runs with longer average fade durations suffer from increased signal outages. The signal outages on some runs are due to a few long fades (these have large \bar{D}_F) while other runs experience a large number of short fades (these have small \bar{D}_F). There is a complete characterization of the channel should include the severity of the fade, the average fade duration, and the signal outage percentage.

To facilitate comparisons with other experiments the average fade duration in meters are included in Tables 8 and 9. The data shows that for $L = 6$ dB the averages of the average fade durations for category II and III runs are 3.3 meters and 6.4 meters, respectively while for $L = 10$ dB they are 2.7 meters and 4.4 meters. As expected, the average fade durations decrease with increasing L , although not by much.

A comparison of these results and the mean fade durations from other experiments is summarized in Table 7. The results of the European L-band experiments are taken from [14] (the highway run is the category I run and the city, run is the category III run) while the results of the Australian L-band experiments were taken from [7] (run 342 is the category II

run and run 409 is the category III run). The fade durations derived from the AMT data are about one-eighth those of the European L-band experiments and about five times those of the Australian L-band experiments for the category III runs. These differences may be explained as follows:

1. Both L-band experiments used antennas with significantly wider beam-widths than the K-band AMT antenna.
2. For the European experiments, the fade threshold L varied from run to run making direct comparisons problematic.

The results suggest that in contrast to the 1 % fade exceedance levels, the average fade durations for the AMT experiments are roughly the same as those of similar experiments at L-band.

5 Summary and Concluding Remarks

The derived probability density model shows that the 1% fade exceedance levels at K-band are much higher than those at L-band while the 10% fade exceedance levels at K-band are lower. This behavior shows that the K-band channel is more likely to be extremely "good" or extremely "bad" than somewhere in between. The characteristics of the cumulative density function are strongly dependent on environment even which lane the vehicle is in. The extremes seem to be much more severe at K-band than what has been reported at L-band. This is due to the increased sensitivity of the AMT K-band system to the time share nature of the multipath and shadowing Contributions to the fading process.

A discrete time model provides insight into the bursty nature of the errors induced by propagation effects on the channel. For a data rate of 9600 bits/sec and a fade threshold of $L = 6$ dB, the average fade duration is on the order of a few thousand bits which corresponds to a fade duration of 2 to 5 meters. The fade durations are typical of those at L-band which suggests that while the K-band fades are more severe than those at L-band, the durations are approximately the same. The discrete time model also provides insight into the signal outage percentages. The signal outages range from $\sim 2\%$ on good runs to as high as 52% on bad runs. Again, the differences between good and bad conditions are exaggerated by the extreme attenuation due to shadowing at K-band together with the rejection of most of I-axis reflections by the narrow-beam antenna.

A complete characterization of the channel should include the fade exceedance levels, the average fade durations, and the percentage of signal outage. All three yield important information which define the requirements for reliable communication on the channel. For example, a large 1 % fade exceedance level is easily overcome if the average fade duration is short.

When K-band is used for mobile satellite communications, care should be taken to choose appropriate coverage environments (e.g. freeways free of line-of-sight obstructions). For environments where frequent line-of-sight obstructions are unavoidable, the 1 % fade exceedance

levels are too severe to be covered by margin in the link budget. The fade durations seem to be on the order of those encountered at L-band suggesting interleaved FEC coding as a possible method for mitigating the effects of fading.

A Multipath Interference

Neglecting the specular component and thermal noise, the pilot tone signal received by the mobile terminal is

$$r(t) = r_{\text{los}}(t) + r_{\text{dif}}(t) \quad (14)$$

$$= D \cos \omega_0 t + \sum_{i=1}^N P_i \cos[(\omega_0 + \Delta\omega_i)t + \phi_i] \quad (15)$$

where P_i is the amplitude of the i -th indirect reflected signal, $\Delta\omega_i$ is the difference in Doppler frequency shifts between the i -th indirect reflected signal and the direct LOS signal, and ϕ_i is difference in phase between the i -th received signal and the direct LOS signal due to the difference in path lengths of the two signals. The amplitudes P_i , the relative Doppler shifts $\Delta\omega_i$, and the relative phases ϕ_i are mutually independent random processes where each ϕ_i is assumed to be uniformly distributed on $[-\pi, \pi]$. The second term in (15) represents the diffuse component which may be expressed as

$$r_{\text{dif}}(t) = \sum_{i=1}^N P_i \cos(\Delta\omega_i t + \phi_i) \cos \omega_0 t - \sum_{i=1}^N P_i \sin(\Delta\omega_i t + \phi_i) \sin \omega_0 t \quad (16)$$

$$= N_c(t) \cos \omega_0 t - N_s(t) \sin \omega_0 t. \quad (17)$$

For N sufficiently large, $N_c(t)$ and $N_s(t)$ are approximated by narrow-band stationary independent Gaussian random processes with zero mean and common variance σ_d^2 . Thus, the received signal power

$$S = (D + N_c(t))^2 + N_s(t)^2 \quad (18)$$

is described by the non-central chi-square probability density function [6]

$$p(S) = \frac{1}{2\sigma_d^2} \exp \left\{ -\frac{D^2 + S}{2\sigma_d^2} \right\} I_0 \left(\sqrt{S} \frac{D}{\sigma_d^2} \right) \quad (19)$$

where $I_0(\cdot)$ is the modified Bessel function of the first kind of zero order. By normalizing the received line-of-sight pilot power to unity

$$D^2 = 1 \quad (20)$$

and defining the Ricean parameter κ as the power ratio of direct to indirect signal powers

$$\kappa = \frac{D^2}{2\sigma_d^2}, \quad (21)$$

$p(S)$ may be parameterized and assume the form

$$p(S; \kappa) = \kappa e^{-\kappa(1+S)} I_0(2\kappa\sqrt{S}). \quad (22)$$

When no line-of-sight signal is present, $D=0$ and the probability density function of

$$\mathbf{S} = N_c(t)^2 + N_s(t)^2 \quad (23)$$

is the well known non-central chi-square pdf [6]

$$p(S) = \frac{1}{2\sigma_d^2} \exp\left\{-\frac{S}{2\sigma_d^2}\right\}. \quad (24)$$

In this case $2\sigma_d^2$ is the mean received signal power S_0 . Since $D=0$ implies $\kappa=0$, the form (24) is a special case of (19). Thus, (24) is usually expressed as

$$p(S;0) = \frac{1}{S_0} \exp\left\{-\frac{S}{S_0}\right\}. \quad (25)$$

Acknowledgments

The research described in this paper was completed at the Jet Propulsion Laboratory, California Institute of Technology, under a contract with the National Aeronautics and Space Administration.

The authors are grateful to Mr. Jim Mesa, Forestry Inspection Foreman for the City of Pasadena, and Mr. Stewart Jessup, C.G.C.S. Brookside Golf Course, for their assistance in identifying foliage along the experiment routes.

References

- [1] B. Abbe and M. Agan. ACTS mobile terminals. to appear in the special issue of the *International Journal of Satellite Communications* on ACTS.
- [2] A. Densmore and V. Jamnejad. A satellite- L - and K_a -band mobile vehicle antenna system. *IEEE Transactions on Vehicular Technology*, VT-42:502- 513, november 1993.
- [3] J. Goldhirsh and W. Vogel. Propagation effects for land mobile satellite systems: Overview of experimental and modeling results. Technical report, NASA Reference Publication 1274, February 1992.
- [4] W. C.-Y. Lee. *Mobile Communications Engineering*. McGraw-Hill, New York, 1982.
- [5] W. Vogel. Propagation considerations in land mobile satellite transmission. Technical Report 105, MSAT-X, 1985.
- [6] J. G. Proakis. *Digital Communications*. McGraw-Hill, New York, second edition, 1989.
- [7] Y. Hase, W. Vogel, and J. Goldhirsh. Fade-durations derived from land-mobile-satellite measurements in Australia. *IEEE Transactions on Communications*, 39(5):664-668, May 1991.
- [8] J. Goldhirsh, W. Vogel, and Y. Hase. Land-mobile-satellite fade measurements in Australia. *IAA Journal of Spacecraft and Rockets*, 29(1):123-128, January-February 1992.
- [9] Y. Okumura, H. Ohmori, T. Kawano, and K. Fukuda. Field strength and its variability at VHF and UHF land mobile services. *Rev. Electr. Commun. Lab.*, 16:825-873, 1968.
- [10] D. Black and D. Reudink. Some characteristics of mobile radio propagation at 836 MHz in the Philadelphia area. *IEEE Transactions on Vehicular Technology*, VT-21:45-51, 1972.
- [11] W. C.-Y. Lee and Y. Yeh. on the estimation of the second-order statistics of log normal fading in mobile radio environment. *IEEE Transactions on Communications*, COM-22(6):869-873, June 1974.
- [12] D. Reudink. Comparison of radio transmission at X-band frequencies in suburban and urban areas. *IEEE Transactions on Antennas and Propagation*, AP-20:470-473, 1972.
- [13] C. L. 100. A statistical model for a land mobile satellite link. *IEEE Transactions on Vehicular Technology*, VT-34(3):122-127, August 1985.
- [14] E. Lutz, C. Cygan, M. Dippold, F. Dolainsky, and W. Papke. The land mobile satellite communication channel - recording, statistics, and channel model. *IEEE Transactions on Vehicular Technology*, 40(2):375-386, May 1991.

- [15] P. H. Hansen and F. Meno. Mobile fading - Rayleigh and lognormal superimposed. *IEEE Transactions on Vehicular Technology*, VT-26(4) :332-335, November 1977.
- [16] H. Suzuki. A statistical model for urban radio propagation. *IEEE Transactions on Communications*, COM-25:673-680, 1977.
- [17] R. Lorenz. Field strength prediction method for a mobile telephone system using a topographical data bank. in *IEEE Conference Publication No. 188*, pages 6-11, 1980.
- [18] J. Goldhirsh and W. Vogel. ACTS mobile propagation campaign. In *Proceedings of the Eighteenth NA SA Propagation Experimenters Meeting (NA PEX XVIII)*, JPL Publication 94-19, pages 135-150. Jet Propulsion Laboratory, 1994.
- [19] J. Castro. Statistical observations of data transmission over land mobile satellite channels. *IEEE Journal on Selected Areas in Communications*, 10(8):1277-1285, October 1992.
- [20] B. Vucetic and J. Du. Channel modeling and simulation in satellite mobile communications systems. *IEEE Journal on Selected Areas in Communications*, 10(8): 1209-1218, October 1992.
- [21] G. Butt, B. Evans, and M. Richharia. Narrowband channel statistics from multiband propagation measurements applicable to high elevation angle land-mobile satellite systems. *IEEE Journal on Selected Areas in Communications*, 10(8):1219-1226, October 1992.
- [22] M. Rice. AMT antenna pointing errors. Technical Report AMT:331.09-95-031, Jet Propulsion Laboratory, July 1995.
- [23] D. Divsalar. Calculation of the Rician parameter for AMT. Technical Report AMT:331.2-90-078 (Internal Document), Jet Propulsion Laboratory, February 1991.
- [24] L. Kanal and A. R. K. Sastry. Models for channels with memory and their applications to error control. *Proceedings of the IEEE*, 66(7):724-744, July 1978.
- [25] S. Berkovits and E. Cohen. A 3-state model for digital error (Distributions). Technical Report ESD-TR-67-73, The Mitre Corporation, Bedford, MA, 1967.
- [26] R. McCullough. The binary regenerative channel. *Bell System Technical Journal*, 47:1713-1735, October 1968.
- [27] P. Trafton, H. Blank, and N. McAllister. Data transmission network computer-to-computer study. In *Proceedings of ACM/IEEE Symposium on Problems in the Optimization of Data Communication Systems*, pages 183-191, Palo Alto, CA, October 1971.

- [28] B. Pritchman. A binary channel characterization using partitioned Markov chains, *IEEE Transactions on Information Theory*, IT-13:221-227, April 1967.
- [29] H. Blank and L. Trafton. A Markov error channel model. In *Conference Record of the IEEE National Telecommunication Conference (NTC)*, pages 15B-1-15B-8, 1973.
- [30] R. Chien, A. Haddad, B. Goldberg, and E. Moyes. An analytic error model for real channels. In *Proceedings of the IEEE International Conference on Communications (ICC)*, pages 15-7-15-12, June 1972.
- [31] P. Varshney and A. Haddad. A Markov gap model with memory for digital channels. In *Proceedings of the IEEE International Conference on Communications (ICC)*, pages 15-24-15-27, June 1975.
- [32] E. Gilbert. Capacity of a burst-noise channel. *Bell System Technical Journal*, 39:1253-1266, September 1960.
- [33] J. G. Kemeny and J. L. Snell. *Finite Markov Chains*. Springer-Verlag, New York, 1976.
- [34] C. Siew and D. Goodman. Packet data transmission over mobile radio channels. *IEEE Transactions on Communications*, VT-38(2):95-101, May 1989.
- [35] S. Rice. Distribution of the duration of fades in radio transmissions: Gaussian noise model. *Bell Systems Technical Journal*, 37:581-615, May 1958.

Table 1: Environmental Characteristics of AMT Propagation Runs

RUN	CAT.	L) IRECTION	TERRAIN	OBSTRUC TIONS
020201	I	West straight	hilly	none
070901	III	south, right lane straight	flat	trees ¹
070903	III	north curved	flat	trees ² : canopies cover road
070905	II	north, right lane straight	flat	trees ¹
070906	III	south curved	flat	trees ² : canopies cover road
070907	III	north, left lane straight	flat	trees ¹
070912	III	south curved	hilly	trees ³ : canopies cover road
070914	III	north curved	hilly	trees ³ : canopies cover road
071016	II	north/south curved	flat	trees ⁴
071017	II	north/south curved	flat	trees ⁴
072405	II	east, left lane straight	hilly	trees ⁵ , utility poles
072406	-II	west, left lane straight	hilly	trees ⁵ , utility poles
072407	II	east, right lane straight	flat	trees ⁶ , utility poles, buildings
072408	II	west, right lane straight	flat	trees ⁷ , utility poles
072409	III	south, right lane straight	flat	trees ¹
072410	II	north, right lane straight	flat	trees ¹
072411	II	South, left lane straight	flat	trees ¹
072412	II	north, left lane straight	flat	trees ¹

¹In order of concentration: Southern Magnolia, Fan & Date Palm, Coastal Live Oak, California Pepper.

²In order of concentration: Coastal Live Oak, Southern Magnolias, Holly Oak.

³In order of concentration: Coastal Live Oak, Holly Oak, California Sycamore Deadora Cedar, California Pepper.

⁴In order of concentration: Oak, Pine, Sycamore, Magnolia, Cedar, Eucalyptus, Palm, California Pepper, Italian Cyprus.

⁵In order of concentration: Italian Cyprus, Palm, California Sycamore, Deadora Cedar

⁶In order of concentration: Ficus (aka Indian Laurel Fig), Date Palm.

⁷In order of concentration: Eucalyptus, Fan and Date Palm.

Table 2: Summary of Best Fit For 20 GHz Data Using The Lutz Model.

RUN	CAT.	A	κ (dB)	μ (dB)	σ (dB)	1% FADE LEVEL (dB)	5% FADE LEVEL (dB)	10% FADE LEVEL (dB)
020201	I	0.000	28.8	-	-	0.4	0.2	0.1
070901	II	0.040	28.4	-11	-21.37	8.0	1.0	1.0
070903	III	0.433	21.1	-20.8	-0.09	>> 30.0	>> 30.0	29.0
070905	II	0.582	21.5	-23.2	7.37	>> 30.0	> 30.0	27.0
070906	III	0.188	23.2	-24.4	9.01	> 30.0	17.5	6.0
070907	II	0.219	23.0	-1.6	10.59	27.5	16.0	7.5
070912	III	0.406	20.9	-19.1	-17.49	>> 30.0	> 30.0	27.0
070914	III	0.394	4.0	-20.3	-0.13	>> 30.0	>> 30.0	> 30.0
071011	II	0.016	18.2	-19.9	1.13	> 25.0	2.0	1.5
071017	II	0.032	17.7	-13.1	6.67	22.2	2.0	1.5
072405	II	0.231	16.2	-13.7	11.14	> 30.0	21.0	11.0
072406	II	0.124	20.3	-2.7	10.38	23.0	7.0	1.5
072407	II	0.343	22.3	-21.0	1.48	>> 30.0	>> 30.0	> 30.0
072408	II	0.145	27.1	-19.8	13.99	21.0	8.0	1.0
072409	II	0.100	23.5	1.4	-37.99	9.5	1.5	1.0
072410	II*	0.548	19.0	-16.3	8.69	>> 30.0	> 30.0	26.5
072411	II*	0.010	19.2	-12.7	6.071	> 30.0	2.0	1.5
072412	II	0.213	19.8	-11.9	3.83	30.0	16.0	9.0

Table 3: Fade Exceedance Results from [8] for L-band with 51° Elevation Angle and Two Receive Antenna Gain Patterns: omni-azimuth/ 55° -elevation for Runs 322,343,359 and 45° -azimuth/ 45° -elevation for Runs 406,409.

		1 %	5 %	10 %
		FADE LEVEL	FADE LEVEL	FADE LEVEL
		(cm)	(dB)	(dB)
Run	CAT.			
Run 322	II	10.0	3.0	1.0
Run 343	III	>15.0	> 15.0	14.0
Run 359	II	10.2	5.5	2.5
Run 406	II	16.5	10.5	7.5
Run 409	II	24.2	15.0	12.0

Table 4: Fade Exceedance Results from [14] for L-band with 43° Elevation Angle and Hemispherical Receive Antenna Gain Pattern.

		1 %	5 %	10 %
		FADE LEVEL	FADE LEVEL	FADE LEVEL
		(dB)	(dB)	(dB)
City	CAT.			
City	III	27.5	23.0	21.0
Highway	I	3.5	2.0	1.5

Table 5: Fade Exceedance Results from [21] for L-, S-, and Ku-bands with 60° Elevation Angle and 64° -azimuth/ 64° -elevation for L- and S-band Receive Antennas; 80° -azimuth/ 80° -elevation for Ku-band Receive Antenna.

		1 %	5 %	10 %
		FADE LEVEL	FADE LEVEL	FADE LEVEL
		(dB)	(dB)	(dB)
	CAT.			
L-band	II	16.5	8.0	5.0
S-band	II	18.5	9.0	6.0
Ku-band	II	27.5	19.5	13.0

Table 6: Fade Exceedance Results from [18] for K-band with 55° Elevation Angle in Texas and 55° Elevation Angle in Maryland; 27° Beamwidth Receive Antenna.

		1 %	5 %	10 %
		FADE LEVEL	FADE LEVEL	FADE LEVEL
		(dB)	(dB)	(dB)
	CAT.			
Bastrop, TX	III	28.0	20.0	15.0
Austin, TX	III	32.0	24.0	21.0
Austin, TX	II	15.0	9.0	7.0
Rt.108, MD	III	24.0	15.0	11.0
RT.295, MD	II	14.0	2.5	2.0

Table 7: Mean Fade Duration Comparisons

	<i>L</i> (dB)	FADE DURATION CATEGORY		
		J	II	III
AMT K-band	6		3.3 m	6.4 m
AMT K-band	10		2.7111	4.4 m
European L-band	variable	17.0111		49.0 m
Australian L-band	5		0.4 m	1.2111

Table 8: Run Summary For 20GHz Data With $L = 6$ dB Using The Gilbert Model for $R_b = 9600$ bits/second.

RUN	CAT.	v (m/s)	π_1	P_{00}	P_{11}	$D_N(b)$	$I_{1, < 6}$	$D_N(m)$	$D_F(m)$
070901	II	13.4	0.015	0.999994	0.998724	162241	784	226.0	1.1
070903	III	11.6	0.337	0.999935	0.999826	15362	5742	18.6	6.9
070905	II	11.6	0.402	0.999911	0.999748	11204	3971	13.5	4.8
070906	III	9.8	0.104	0.999991	0.999646	112979	2824	115.3	2.9
070907	II	11.6	0.083	0.999997	0.999571	337618	2334	408.0	2.8
070912	III	8.5	0.409	0.999958	0.999899	325418	9892	288.1	8.8
070914	III	7.6	0.528	0.999957	0.999888	23435	8933	18.5	7.1
071016	II	11.6	0.045	0.999993	0.999678	142477	3107	172.2	3.8
071017	II	11.6	0.042	0.999994	0.999669	174611	3019	211.0	3.6
072405	II	14.3	0.226	0.999948	0.999800	19369	5010	28.8	7.5
072406	II	13.4	0.049	0.999995	0.999305	194135	1439	271.0	2.0
072407	II	12.5	0.256	0.999961	0.999744	25638	3908	33.4	5.1
072408	II	13.8	0.053	0.999991	0.999411	105727	1698	152.0	2.4
072409	II	13.8	0.012	0.999992	0.997759	125127	446	179.9	0.6
072410	II	14.3	0.391	0.999809	0.999686	5237	3187	7.8	4.7
072411	II	15.2	0.013	0.999995	0.999367	219951	1580	348.2	2.5
072412	II	14.3	0.123	0.999973	0.999475	37064	1905	55.2	2.8

Table 9: Run Summary For 20GHz Data With $L = 10$ dB Using The Gilbert Model for $R_b = 9600$ bits/second.

RUN	CAT.	v (m/s)	π_1	p_{00}	p_{11}	$\overline{D_N(b)}$	$\overline{D_F(b)}$	$\overline{D_N(m)}$	$\overline{D_F(m)}$
070901	II	13.4	0.008	0.999994	0.994261	173119	174	241.6	0.2
070903	III	11.6	0.298	0.999935	-0.999716	15403	3516	18.6	4.2
070905	II	11.6	0.329	0.999928	0.999693	13823	3256	16.7	4.8
070906	III	9.8	0.085	0.999993	0.999625	144765	2669	147.8	2.7
070907	II	11.6	0.061	0.999979	0.999403	48104	1675	58.1	2.0
070912	III	8.5	0.362	0.999951	0.999798	20475	4942	18.1	4.3
070914	III	7.6	0.464	0.999940	0.999877	16661	8115	13.2	6.4
071016	II	11.6	0.037	0.999993	0.999655	139952	2902	169.1	3.5
071017	III	11.6	0.031	0.999995	0.999585	195219	2407	235.9	2.9
072405	II	14.3	0.101	0.999957	0.999547	23059	2208	34.3	3.3"
072406	III	13.4 13.4	0.037 0.037	0.999997	0.998694	395585	766	552.2	1.1
072407	III	12.5	0.239	0.999961	0.999730	25897	3700	33.7	4.8
072408	II	13.8	0.038	0.999990	0.999383	100063	1620	143.8	2.3
072409	II	13.8	0.008	0.999991	0.995307	110503	213	158.8	0.3
072410	II	14.3	0.339	0.999922	0.999613	12859	2587	19.2	3.8
072411	II	15.2	0.010	0.999996	0.998246	227516	570	3(X).2	0.9
072412	II	14.3	0.095	0.999977	0.999473	44086	1896	65.7	2.8

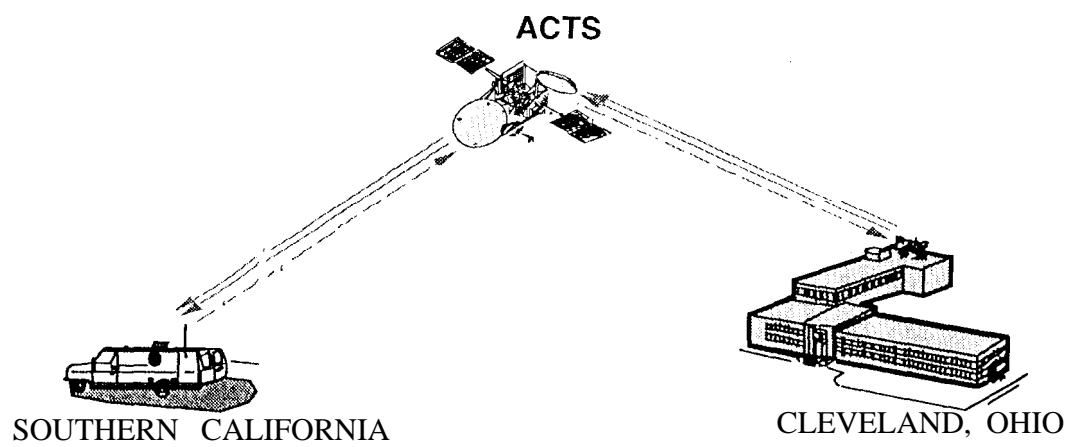


Figure 1: ACTS Mobile Terminal System Configuration

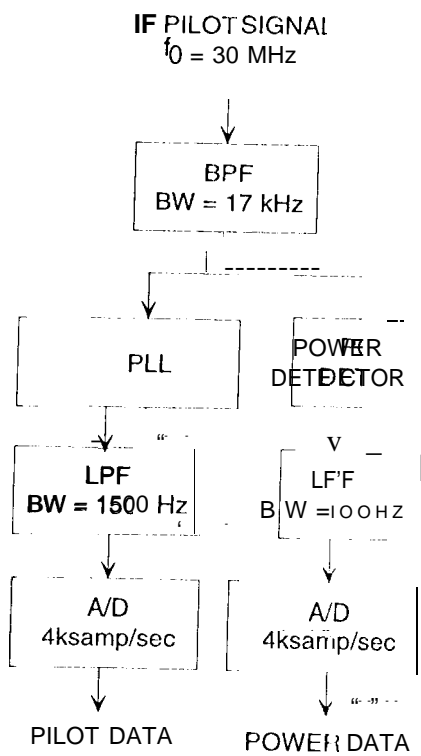


Figure 2: AMT Data Acquisition System Block Diagram

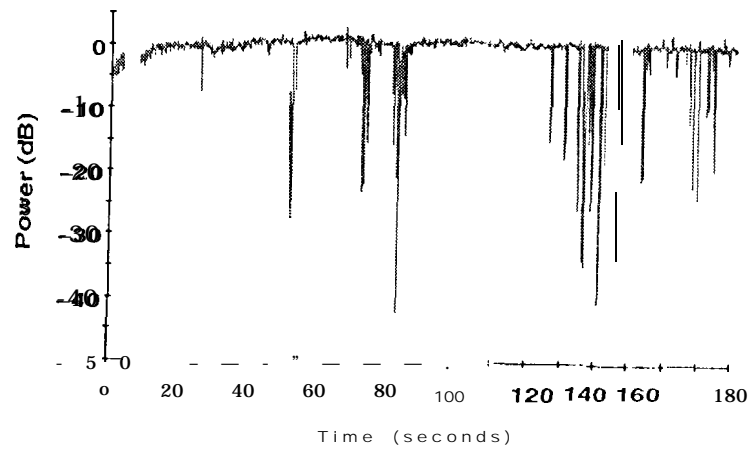


Figure 3: Received Pilot Power vs. Time for Run 072406

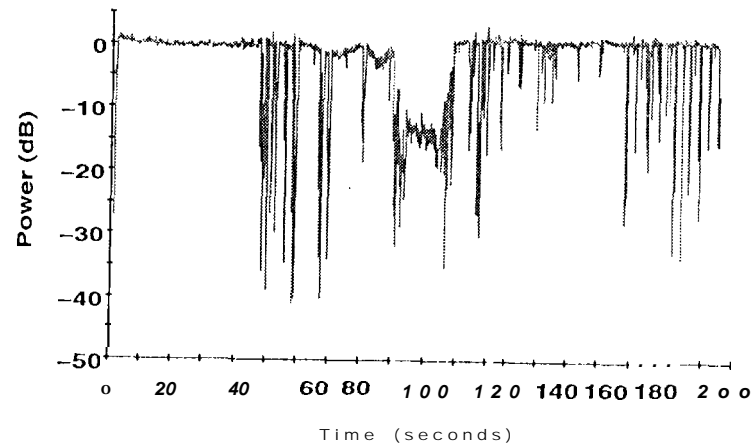


Figure 4: 1 Received Pilot Power vs. Time for Run 072412

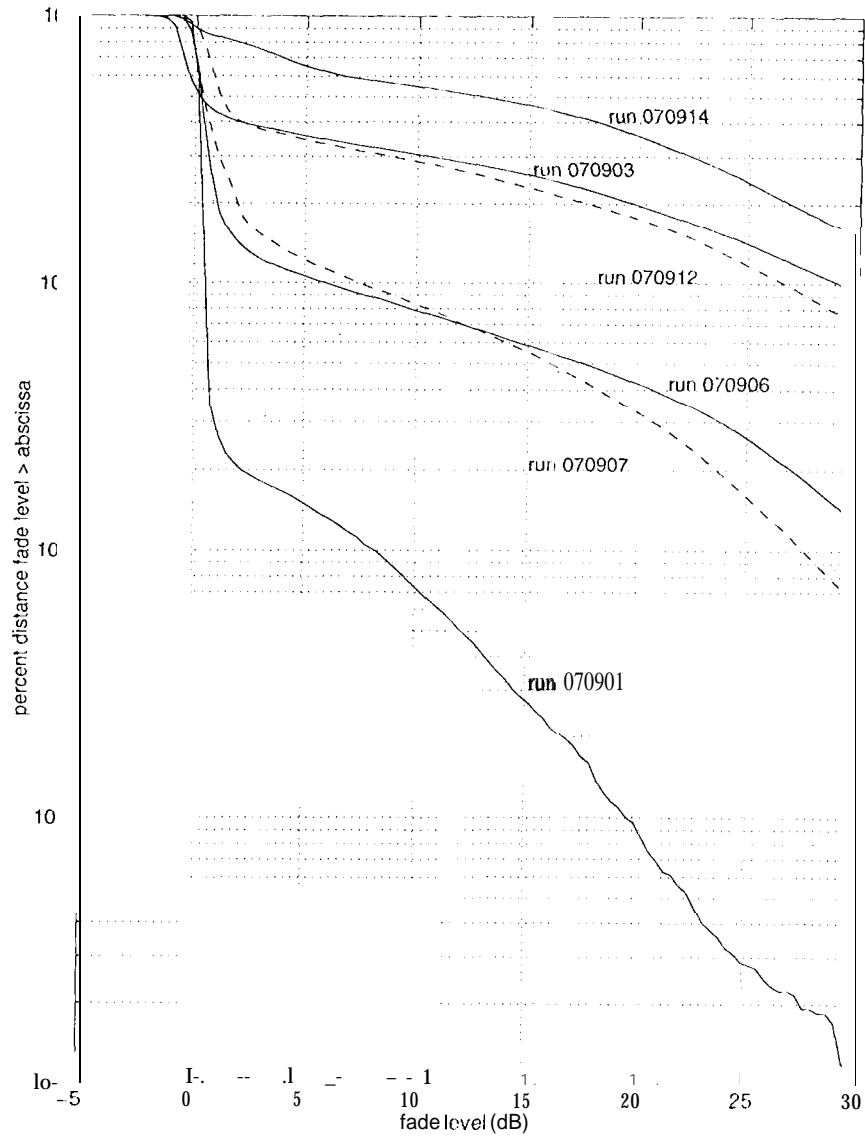


Figure 5: Cumulative Fade Depth Distribution for Representative Runs

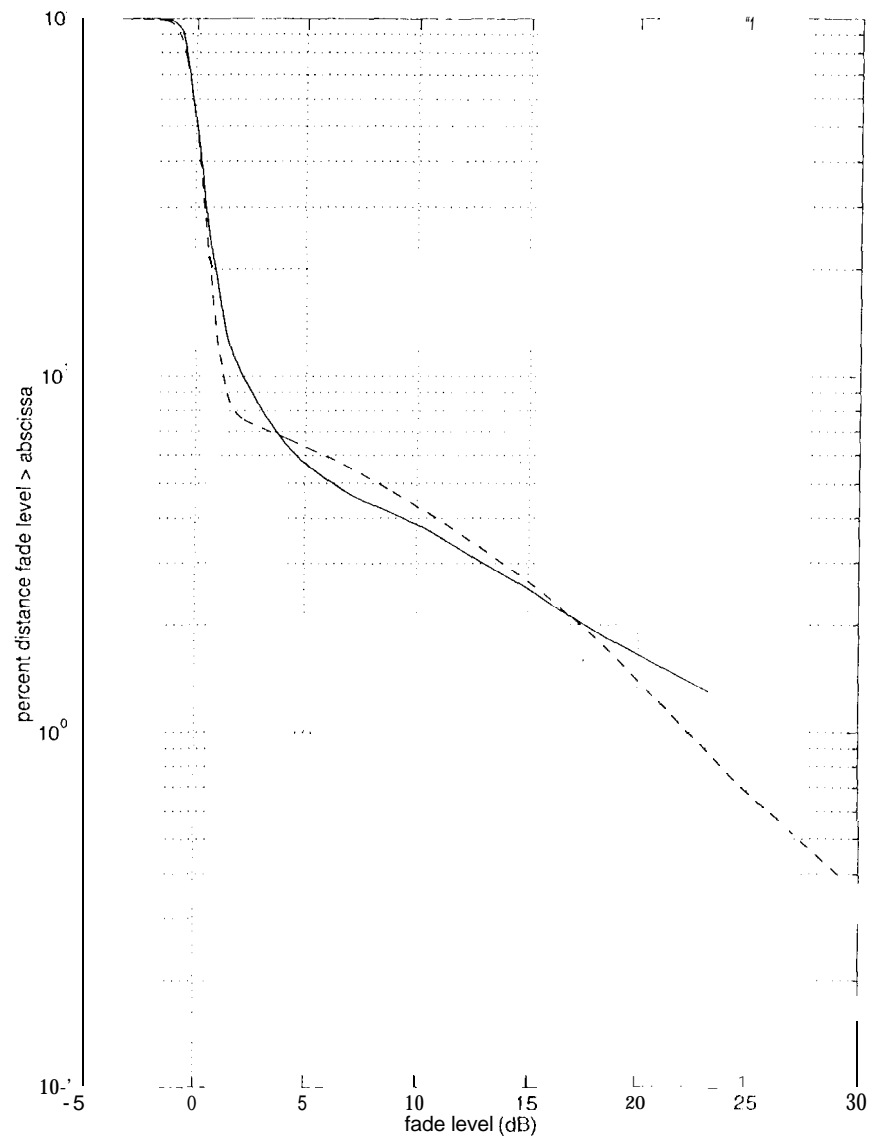


Figure 6: Cumulative Fade Depth Distribution for Run 072406: Solid Line is the Histogram Generated by the Data, Dashed Line is the Least Squares Curve Fit Using 4.

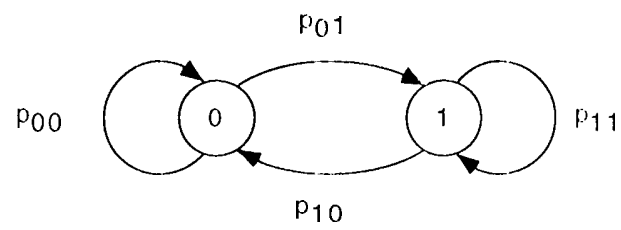


Figure 7: Two State Markov Chain Model of a Burst Error Channel.

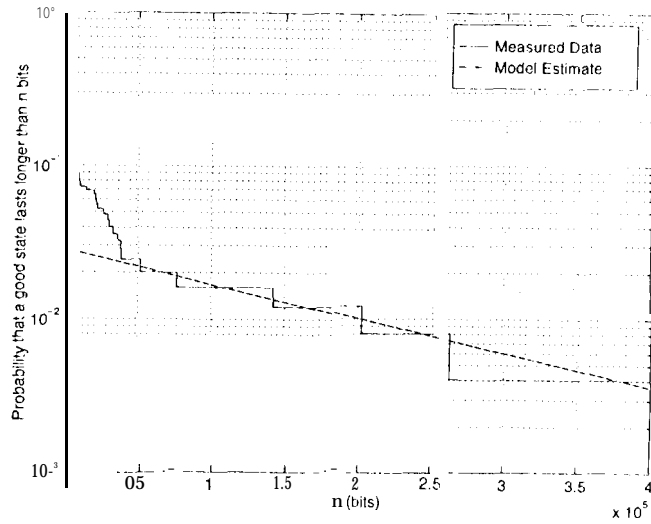


Figure 8: Histogram of the Cumulative Distribution of $D_N(b)$ for Run 072406.

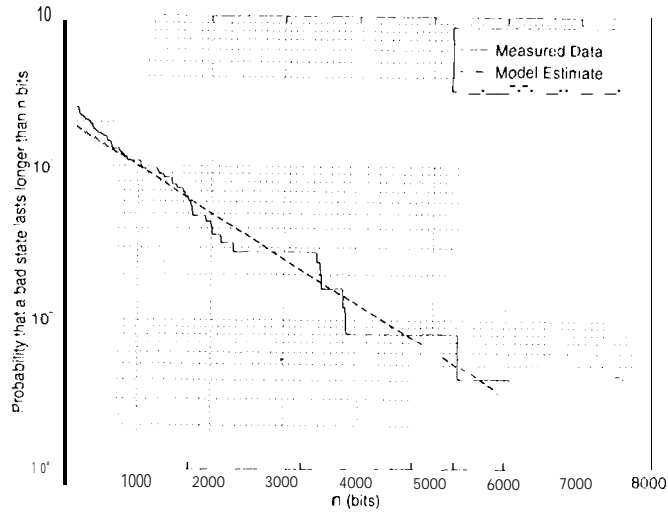


Figure 9: Histogram of the Cumulative Distribution of $D_F(b)$ for Run 072406.

on the Keck 10-m spread over ~ 142 pixels. Thus, assuming **uncorrelated** errors in relative pixel positions, the required **centroid** accuracy for each pixel is $0.0024 \times \sqrt{142} = 0.029$, well within current capabilities (Monet et al. 1992).

Systematic errors in pixel locations due to, for example, step and repeat errors in the CCD fabrication, also introduce errors into the **astrometric** analysis. Shaklan & Pravdo (1994) discuss a method to calibrate such systematic errors. Shaklan & Pravdo (1994) and Shaklan et al. (1995) have demonstrated calibration accuracies in excess of our requirements. Buffington et al. (1990) has shown that CCD photometric and dimensional stabilities are more than adequate for this experiment. Thus σ_{ccd} is negligible.

6.4 Optical Aberrations

Astrometric accuracy can be limited by optical aberrations, especially distortion (Gatewood 1992). For large apertures and small fields of view aberrations are small. For example, Figure 5 shows the as-designed distortion for the Keck 10 m across the CCD field of view. The telescope has low intrinsic distortion and also low sensitivity to motion of the secondary mirror. These effects are negligible compared to other sources of error.

Another issue for the Keck 10-m is the effect of the primary segments on astrometry. Astrometric performance is insensitive to aberrations on the primary since all stars are affected in the same way. The Keck segments are actively aligned to 50 mas . For 36 segments this implies that centroid motion due to one segment will be $1400 \text{ } \mu\text{as}$. Therefore to achieve astrometric accuracy of

-1 0°/0 of the overall **centroid** motion, This is expected to be the case since segment misalignments are well within the seeing disk diameter. Thus σ_{ab} is also negligible.

7. PROGRAM DESCRIPTION AND ANTICIPATED RESULTS

7.1 Telescopes and Sites

We compare the performance of three telescopes and sites to determine the effect of telescope diameter and other parameters on a **planet** detection program. We use our 5-m results and extrapolate to two other telescopes: the Palomar 1.5-m and the Keck 10-m, Table 3 lists the relevant parameters for the comparison. Most of the discussion will relate to a program with the 10-m telescope since it has by far the most potential.

For the three telescopes considered the fields of view are chosen by balancing two competing effects which relate to measurement noise and the ability to model the field. Smaller fields have fainter reference stars and thus have more photometric noise. Larger fields have brighter reference stars but more atmospheric noise because the atmospheric noise in the relative astrometric signal between stars is proportional to the stellar separation in the small angle limit (§ 1.2). Larger fields also have more reference stars. This allows a better **determination** of the field model (e.g. Eichhorn & Williams). A minimum of four reference stars is required to determine a linear model of the field and solve for the reference star **parallaxes** and proper motions. For small fields and small optical aberrations a linear model is usually sufficient. In the cases where a quadratic model gives better

results at least seven reference stars are required. At the Keck telescope a field of view of $84''$ (Table 3) yields an average of 8.6 reference stars with $V \leq 21$ at $b'' = 30^\circ$ (Allen 1973). A limiting magnitude of $V = 21$ was chosen because these are the faintest stars that can be used as statistically significant reference stars in the observations.

Reference stars form a reference frame with an effective brightness which depends on the intensity and spatial distribution of the stars. Monte-Carlo simulations of reference fields show that the effective brightness is 5 times fainter than the summed light of the frame (see Appendix). For the Keck telescope, this translates into an effective reference frame magnitude of $V = 19$. The reference frame is effectively $V = 17$ at the 5-m telescope and $V = 16$ at the 1.5-m. In the analysis discussed below the reference frame photometric centroid noise, σ_p , is computed by fitting a Gaussian profile to a star with magnitude equal to the effective reference frame magnitude. The Gaussian was fitted with a weighted least-squares algorithm, where the weight of each pixel in the sum of the squared residuals is given by the summed variances of photon noise, detector noise, and sky background. The algorithm is discussed in detail by Stone (1989).

For purposes of comparison between the 10-, 5-, and 1.5-m telescopes, we choose fields of view that have the same average number of reference stars. The Keck field is the largest that fits on a current large-format CCD. The linear sizes of the 5-m and 1.5-m fields are smaller. In all three cases, the atmospheric noise is substantially worse than the photometric noise and is the limiting factor for astrometric accuracy. For example, the atmospheric noise at the 5-m as derived from our results is $\sigma_a = 150 \mu\text{as}/\sqrt{\text{hr}}$, while the photometric noise is $\sigma_p = 71 \mu\text{as}/\sqrt{\text{hr}}$.

7.2 Target Stars

As shown in (8) the astrometric signal depends inversely on the distance to the star. Thus nearby stars are the best candidates to search for planets using this method. Our source catalog for stars within 25 pc of the Sun is the *Preliminary Version of the Third Catalogue of Nearby Stars* or *CNS3* (Gliese & Jahreiss 1993). *CNS3* contains 3802 stars including 3 B, 73 A, 264 F, 486 G, 772 K, and 1097 M stars. We also treat 639 stars with color class “m” as M stars based upon their colors and absolute luminosities. We have spectroscopically verified that a number of these stars are M stars (Pravdo et al. 1995). Stellar distances are determined from the given trigonometric parallaxes or in some cases photometric and spectroscopic parallaxes. Stellar masses are determined using the relation:

$$\log \left(\frac{M_S}{M_\odot} \right) = 0.118 (4.75 - M_{bol}) \quad (12)$$

with the stellar bolometric magnitude, M_{bol} , taken from the spectral type, luminosity class, and bolometric corrections (Allen 1973). A minimum mass of $0.1 M_\odot$ is assumed. For stars where the luminosity class or subtype is not given, we assume luminosity class V and subtype 0.5. Stars with color types of “m” are assumed to be M5 dwarfs for the mass estimates. This is consistent with their absolute luminosities.

We begin with the 3229 *CNS3* stars which have ≥ 300 mas for a Jupiter-mass planet and $T \leq 10$ yr. Planets around a subset of these stars could be detected at 3σ with the achieved precision but as described below (§7.2) much more time than the survey allows would be required to observe

all of them, We **further** restrict this sample. First, to limit the effects of DCR (§3.2) we use a $\pm 45^\circ$ swath in declination around the zenith of the ground-based observatory site. Second, to insure enough reference stars in each field (§6.1), we limit the galactic latitude of the target stars to $b'' \leq 30^\circ$. Last, we introduce a telescope- and detector-dependent V magnitude lower limit to prevent image saturation. The magnitude limits are listed in Table 3 and correspond to the brightest stars that can be observed in a fast-readout region of the CCD. This results in 838 candidates, consisting of 2 A, 25 F, 105 G, 174 K, 330 M, and 202 m stars. Figure 6 shows the astrometric signals for these stars assuming Jupiter-mass planets in 10-year orbits, plotted in order of spectral type and sub-type, with each sub-type sorted by astrometric signal magnitude.

We keep some known binaries in our target list (see below). Only those with small apparent separations are removed, The minimum real separation for the remaining binaries is then 745 au. Some short-period binaries will be discovered by this survey and eliminated when appropriate. Long-period binaries both known and discovered are not expected to be different from single stars in the properties of their planetary systems. In studies of a subset of *CNS3* less than 3% of the stars were in long-period binary systems (Wasserman & Weinberg 1991).

7.3 Anticipated Results

We now present results of an end-to-end model of planet detection using the target stars, reference fields, and measurement errors discussed above. To observe a statistically significant sample of stars requires that a telescope be dedicated at least in part to this program: we assume a minimum of 40 nights yr^{-1} . Since the survey is time- and not source-limited the number of stars surveyed increases

almost linearly with available observing time. We assume a bright sky (background $V = 20$ mag as^{-2}) for this analysis. The observing efficiency due to bad weather and other effects, is chosen to be 50%, resulting in a net observing time of 160 hr yr^{-1} . The program will last for 10-20 yr, a necessity considering the range of orbital periods in the search. Target stars will be observed twice per year but not evenly spaced. This sampling imposes a lower limit to the period search of $T \gtrsim 1 \text{ yr}$. The DCR calibration observations will be performed infrequently and do not add much overhead to the program. They could be done at an alternate site.

The observation time per target determines the statistical significance of any detection as well as the range in parameter space over which that significance is valid. Since we are searching for planets for which the periods are unknown, each target should be observed long enough so that an important range in that parameter space is sampled. It is incomplete to say that a star has been searched for planets without indicating the range of periods (or semi-major axes) for which the search is valid. We have chosen semi-major axes parameter space to display the results because it maybe the parameter with the most physical interest. If, as suggested by Boss (1995), the radius at which gas giants form is 4-5 a.u. independent of stellar temperature or mass for masses as low as $0.1 M_{\odot}$, then it will be crucial for any observing program, regardless of the stellar sample, to explore this area of parameter space. It is, of course, directly related to orbital period parameter space.

We examine two potential programs: each searches a statistically significant number of stars (≥ 100) but the first emphasizes “Solar-class” spectral types, with an average mass of $0.82 M_{\odot}$, while the second emphasizes star numbers and contains mostly M-type stars. Figure 7 shows the detectable (30) semi-major axes (shaded regions) for the Solar-class stars observed with the 10-, 5-, and 1.5-m telescopes in a 10-yr program. The number of stars is limited to 100 because the Solar-class spectral

types are more massive, have lower signals, and thus each take more observing time than M stars. For this survey $\sigma_o = 100 \mu as$ which is calculated from (11) with $\sigma_a = 85 \mu as \sqrt{hr}$, $\sigma_p = 41 \mu as \sqrt{hr}$, $\sigma_{DCR} = 66 \mu as$, $t = 1.6$ hr, and the other quantities negligible. We assume a 2000 Å bandpass and a 0.35 system throughput.

The target stellar types distribution is listed in Table 3. The Figure and Table demonstrate the utility of a larger aperture: in equal programs the 10-m observes more Solar-like stars, 31 G stars compared to 11 for the 5-m, 2 for the 1.5-m, and covers a larger area of semi-major axes parameter space for each star. Figure 8 shows the coverage gain in semi-major axes space with time, if the program is extended beyond 10 years, After 20 years with the 10-m telescope, the space is searched to 10 au. for nearly the entire sample.

Table 4 lists the 100 candidate target stars, their expected astrometric signals (Sig1O) and orbits (Orb 10) for Jupiter-mass planets in 10-yr orbits, visual magnitudes, galactic latitudes (a measure of the number of reference stars), distances, inferred masses, spectral types, and other names and comments. The 6 known binary stars in this list (e.g. Poveda et al. 1994) have separations which are between 745 -4200 au., large compared to the orbits that we are searching. Most of the comments in Table 4 are from Gliese & Jahreiss. We have updated the information with new referenced data where available.

The alternate program emphasizes number of stars observed rather than a distribution of spectral types. In this case the 10-m telescope can observe 574 stars, mostly of type M (Table 3). With either program, if there are no detections we can conclude that Jupiter-mass planets are uncommon in the samples.

Finally we could search for lower mass planets with a more limited sample and reduced parameter space coverage. For example, a 10-m, 40 night yr^{-1} , 10-yr program could detect 43 Saturn-mass planets around 2-G, 8-K, and 33-M stars, or 5 Uranus-mass planets around M stars. For the later survey the maximum semi-major axes are only 3.2 au.

8. CONCLUSIONS

We have described programs that allow us to make statistically significant surveys of nearby stars for Jupiter-mass planets. The experiment uses an existing ground-based telescope and a CCD camera. Notice that while this program requires careful, continuing long-term calibration, it does not place extraordinary requirements on any one of the random sources of astrometric noise. The final error per observation, $106 \mu\text{as}$, is a factor of 20-40 better than currently obtained with smaller apertures. Larger apertures improve averaging of atmospheric turbulence ($\sim D^{-1/3}$), have smaller fields-of-view with lower noise, and provide a better photometric SNR.

The number of stars, ≥ 100 , in the 40 night yr^{-1} survey, is important because one expects to detect several Jupiter-mass planets in so large a sample if the canonical model of solar system formation is correct. Systems with detected Jupiter-mass planets will be prime targets for terrestrial planet searches. If no Jupiter-mass planets are found in a sample of 100 “solar-like” stars, we can conclude that there is only a 3×10^{-5} probability that gas-giant planets as large or larger than Jupiter form in at least 10% of the systems. Since we do not search the same areas of semi-major axes parameter space for each star this conclusion is an approximation.

There is another unknown for a program in which mostly low-mass M stars are searched. Theoretical modeling has yet to answer the question whether such stars, 2.5-10 times less massive than the Sun, can have Jupiter-mass planets, Jupiter contains **approximately** 0.001 of the present solar system mass, Jupiter-mass planets around the survey stars would contain 0.0025-0.01 of the system **mass**.

In a program of searches for planetary systems similar to one described above, gas-giant planets can be detected. Furthermore, the absence of detectable Jupiter-mass planets would begin to put pressure on the theory that planetary systems like the solar system are common, at least for sampled stars.

We acknowledge Mark Colavita, George Gatewood, Anthony Gleckler, Hiroshi Kadogawa, Eugene Levy, David Monet, and Michael Shao for useful discussions.

REFERENCES

- Allan, D. W. 1966, *Proc. IEEE*, 54, 221
- Allen, C. W. 1973, *Astrophysical Quantities*, (Ethylene Press: London)
- Anthony-Twarog, B.J. et al. 1990. *A J*, 99, 1504
- Black, D. C. & Matthews, M. S. 1985, *Protostars and Planets II*, (U. of Arizona Press: Tucson, Space Science Series)
- Black, D. C. & Scargle, J. D. 1982, *Ap J*, 263, 854
- Boss, A. P. 1995, *Science*, 267, 360
- Boss, A. P. & Yorke, H. W. 1993, *ApJ*, 411, 1.99
- Buffington, A. et al. 1990, *P A S P*, 102, 688
- Burke, B. F. et al. 1993, *TOPS: Toward Other Planetary Systems*, Solar System Exploration Division Report, NASA publication.
- Cochran, W. D. et al. 1991, *Ap J (Letters)*, 380, L35
- Colavita, M. M. 1994, *A Ap*, 283, 1027
- Dekany, R. et al. 1994, *Ap Sp Sci*, 212, 299
- Eichhorn, H. K. & Williams, C. A. 1963, *A J*, 68, 221
- Gatewood, G. 1987, *A J*, 94, 213
- Gatewood, G. 1991, *B AA S*, 23, 1433
- Gatewood, G. 1992, in *Astrometric Imaging Telescope 1991 Final Report* (ed. S. Pravdo, JPL publication D-965 1), 85
- Gil, J. A. et al. 1993, *A, Ap.*, 271, L17

- Gliese, W. & Jahreiss, H. 1993, Preliminary Version of the Third Catalogue of Nearby Stars (*CNS3*), preprint
- Henry, T. et al. 1994, *AJ*, 108, 1437
- Hufnagel, R. E. 1974, Digest of Technical Papers, Topical Meeting on Optical Propagation through Turbulence, Optical Society of America, Washington, DC, p. Wal
- Jacoby, G. H. et al. 1984, *ApJ Suppl*, 56,257
- Janesick, J. et al. 1989, in *CCDs in Astronomy*, A. S. P. Conference Series No. 6
- Latham, D. W. et al. 1989, *Nature*, 339, 38
- Levy, E. H. et al., 1992, *Protostars and Planets* 111, (U. of Arizona Press: Tucson, Space Science Series)
- Lindgren, L. 1980, *A Ap*, 89, 41
- Marcy, G. W. et al. 1993, *Remote Sensing Rev.*, 8, 205
- Marsh, K. A. & Mahoney, M. J. 1992, *Ap J*, 395, L115
- _____.1993, *Ap J*, 405, L71
- McCarthy, J. K. 1994, *Proc.SPIE*, 2198, 163
- McMillan, R. S. et al. 1994, *Ap.SpSci*, 212,271
- Monet, D. et al. 1992, *A J*, 103, 638
- Monet, D. & Dahn, C. C. 1983, *A J*, 88, 1489
- Peale, S. J. 1993, *A J*, 105, 1562
- Poveda, A, et al. 1994, *Rev Mex A Ap*, 28, 43
- Pravdo, S. H. et al. 1995, in preparation
- Press, W. H. et al. 1989, *Numerical Recipes*, (Cambridge: Cambridge University Press)

- Safronov, V. S. 1969, Evolution of the Protoplanetary Cloud and Formation of the Earth and the Planets (Moscow: Nauka)
- Safronov, V. S. & Ruskol, E. L., Ap Sp Sci, 212, 13 “
- Shaklan, S. et al. 1994a, Ap. Sp.Sci., 212,453
- Shaklan, S. & Pravdo, S. H. 1993, S. P. I. E, 1945, 50S
- Shaklan, S. & Pravdo, S. H. 1994, S. P. I. E., 2198, 1227
- Shaklan, S. et al. 1995, AO, in press
- Shao, M. & Colavita, M. M. 1992, A Ap, 262,353
- Smith, B. A. & Terrile, R. J. 1984, Sci, 226, 1421
- Stone, R. C. 1989, A. J., 97, 1227
- Stubbs, C. W. et al. 1993, Proc. S P I E, 1900, 121
- Wasserman, I. & Weinberg, M. D. 1991, Ap J, 382, 149
- West, F. R. 1967. Ap J (Suppl), 14, 384
- Wolszczan, A. & Frail, D. A, 1992, Nature, 355, 145

Table 1. Stars Observed in NGC 2420

I.D.	x (arcsec)	y (arcsec)	V	B-V	R_{eff}
1116	46	19.4	13.68	-0.003	16.24
2108	33.5	17.1	14.48	0.433	-0.49
2111	19.1	18.7	14.27	0.433	-0.45
2116	9.5	16.1	14.57	0.419	0.62
2119	-3.2	5.7	14.56	0.424	0.54
2120	0	0	14.5	0.417	1.57
2114	17.1	3.4	14.28	0.469	-0.77
2127	8.8	-11.4	14.51	0.432	0.55
2128	14.6	-15.7	15.37	0.502	-1.5
2129	19.2	-16.1	15.65	0.534	-2.52
2122	-24.1	1.1	14.49	0.866	-11.7
2225	-32.5	-4.7	15.98	0.485	-1.58
2226	-41.3	-8.6	15.05	0.445	-0.39
2227a	-36.3	-16.4	14.62	0.41	0.43
J	-45.5	24.9	13.95	0.433	-0.54

Table 2. RMS Photometric Bias and Frame-to-Frame Centroid Noise

Star	Photon Noise ^a	RA Noise ^a	Dec Noise ^a	RA Noise ^b	Dec Noise ^b
1116	0.19	1.25	2.05	0.12	0.37
2108	0.24	0.52	0.86	0.18	0.59
2111	0.25	0.42	0.75	0.05	0.29
2116	0.30	0.60	1.16	0.08	0.43
2119	0.26	0.55	1.19	0.35	0.32
2120	0.24	0.77	1.10	0.25	0.32
2114	0.22	0.49	0.65	0.13	0.95
2127	0.29	0.57	0.89	0.06	0.23
2128	0.51	0.72	1.47	0.40	0.30
2129	0.62	0.56	2.81	0.33	0.66
2122	0.23	0.52	0.76	0.07	0.10
2225	0.86	1.58	1.50	0.19	0.27
2226	0.40	1.12	1.49	0.40	0.41
2227a	0.30	0.94	1.40	0.31	0.36
J	0.20	0.70	1.09	0.16	0.35

^a mas rms in 1 min exposures

^b mas rms in 10 min integrations

Table 3a. Telescope Comparisons--Specifications

Primary Diameter				1.5 m	5 m	10 m
Image Scale ($as/30\text{ }\mu\text{m-pix}$)				0.476	0.078	0.042
Field-of-View Diameter (as)				178	133	84
Faintest Reference Star V				18	19	21
Number	Ref.	Stars	($b^{\text{II}}=30^{\circ}$)	8.6	8.6	8.6
Effective Ref. Frame V				16	17	19
Sky (bright sky mag as^{-2})				19	19	20
Brightest Target Star V				3.2	4.5	4.5
Seeing FWHM (as)				1.0	1.0	0.5

Table 3b. Telescope Comparisons-- “Solar-Class” Search Results

Primary Diameter				1.5 m	5 m	10 m
Stars	Searched	Total		50	100	100
		F		0	1	13
		G		2	11	39
		K		5	23	48
		M		43	65	--
Minimal	Outer	A.U.	Searched	3.5	4.3	4.6

Table 4

Target Stars for the 10-m "Solar-Class" Survey

	Star	Spectral Type	Sig10 (μ as)	Orb10 (au.)	b ^{II} (deg.)	V	D (pc)	Mass (Mo)	Giclas	LHS	Vyss. UGPMF	Other
1	Gl 306	F3 V	451	4.8	18.7	5.6	18.2	1.12				
2	Gl 692	F5 V	444	5.1	4.2	4.9	16.7	1.31				
3	LT 3317	F6 v	530	4.7	18.9	5.8	16.7	1.01				
4	HD 219623	F7 V	402	4.9	-7.1	5.5	19.6	1.20				LTT 16B41
5	Gl 297.2A	F7 V	378	5.0	10.6	5.5	20.5	1.23				Binary 92" sep.
6	Gl 764.2	F7 V	386	5.0	-16.6	5.5	20.0	1.23				
7	Gl 41	F8 v	611	4.9	-1.7	4.8	13.2	1.16				
8	HD 11007	F8 v	395	4.9	-28.7	5.8	20.4	1.16				LTT 10624
9	Gl 202	F8 Ve	509	4.9	-10.3	5.0	15.3	1.21				
10	Gl 364	F9 IV	692	4.8	21.5	4.9	12.2	1.08				
11	Gl 231.1A	F9 V	527	4.7	-5.2	5.7	16.4	1.04				Binary 95" sep.
12	BS 2883	F9 V	369	4.9	4.9	5.9	21.7	1.16				
13	Gl 654.1	F9 V	434	4.7	23.8	6.0	19.6	1.07				
14	HD 30090	G0	489	4.5	-1.9	6.5	19.2	0.92				
15	Gl 245	G0 V	543	4.8	17.5	5.2	15.1	1.12				PSI(5) Aur
16	Gl 252	G0 V	506	4.7	12.1	5.7	16.9	1.05				
17	GJ 1095	G0 V	486	4.8	23.5	5.6	17.2	1.09				5S 2721
18	HD 187923	G0 V	444	4.7	-7.8	6.1	19.6	1.03				LTT 15805
19	Gl 836.7	G0 V	614	4.5	-28.3	5.9	15.1	0.93				
20	HR 8455	G0 V	535	4.6	-29.1	6.2	17.2	0.94				
21	Gl 92	G0 Ve	879	4.6	-25.4	4.9	10.2	0.99		154		BS 660 DEL Tri SBO (A&A 195, 129)
22	Gl 616	G1 V	556	4.7	29.2	5.5	15.4	1.06		3171		
23	Gl 779	G1 V	527	4.7	-7.6	5.8	16.6	1.02		3515		
24	Gl 67	G1.5 V	593	4.9	-19.3	4.9	13.7	1.15		1284		
25	HD 224465	G2	434	4.6	-11.5	6.6	21.3	0.94				LTT 17065
26	Gl 197	G2 IV-V	529	5.0	1.5	4.7	14.4	1.26		1753		IAM Aur
27	HD 225239	G2 V	418	4.7	-27.2	6.1	20.4	1.06		1013		LTT 10009 LFT 4
28	GJ 1085	G2 V	527	4.6	-15.8	6.0	16.9	0.99				LTT 2380 BS2007
29	Gl 230	G2 V	547	4.5	-3.5	6.4	17.6	0.89				
30	Gl 708.4	G2 V	432	4.7	24.9	6.3	20.4	1.01				
31	Gl 327	G3 V	926	4.3	24.2	6.0	11.3	0.78				
32	Gl 209	G4 IV-V	653	4.1	-6.0	7.7	17.8	0.67	G100-O27	6		
33	Gl 262	G4 V	473	4.7	15.3	5.9	18.2	1.05		1893		

Table 4

Target Stars for the 10-m "Solar-Class" Survey

(cont'd)

	Star	Spectral "Type	Sig10 (μ as)	Orb10 (au.)	b" (deg.)	V	D (pc)	Mass (M _o)	Giclas	LHS	Vyss. UGPMF	Other
34	HD 12545	G5	1180	3.6	-25.0	8.4	12.8	0.45				
35	HD 21809	G5	756	4.1	-14.7	7.3	15.4	0.67				
36	HD 68835	G5	1017	3.9	23.0	7.3	12.5	0.58				
37	Gl 160	G5 V	500	4.7	-22.1	5.9	17.4	1.03				
38	BS 2225	G5 V	591	4.4	-18.5	6.4	16.4	0.88				
39	Gl 722	G5 V	675	4.5	-6.8	5.9	13.9	0.92				
40	Gl 746	G5 V	540	4.6	4.1	6.1	16.8	0.97				
41	Gl 822.2	G5 V	780	4.1	-16.1	7.0	14.5	0.70				
42	Gl 703	G6	1112	3.5	16.8	8.7	13.9	0.43				
43	Gl 302	G7.5 V	790	4.4	12.8	6.0	12.6	0.84		245		
44	Gl 759	G8 Iv	486	5.0	-1.9	5.2	15.6	1.27		3463		
45	Gl 777 A	G8 Iv-v	485	4.9	-0.7	5.7	16.7	1.15		3510		Binary 178 sep.
46	Gl 295	G8 v	510	4.4	27.0	7.0	19.4	0.85		242		
47	Gl 641	G8 v	599	4.4	26.1	6.6	16.5	0.85	GOI 9-004	426		
48	GJ 1233	G8 v	549	4.3	20.0	7.0	18.5	0.82	G229-026	6		
49	Gl 754.2	G8 v	558	4.5	10.9	6.3	16.7	0.93				
50	Gl 113.1	G9 e	869	4.1	-25.4	6.8	12.8	0.71				W An SBO (A&A 19S,129)
51	Gl 668.1	G9 V	906	4.2	17.3	6.3	11.8	0.76				
52	Gl 793.1	G9 V	513	4.4	1.2	7.1	19.6	0.83	G209-035			
53	Gl 227	K0 e	679	4.3	-2.5	6.8	15.3	0.79				
54	Gl 75	K0 V	965	4.4	1.7	5.6	10.3	0.85		1297		
55	Gl 654.2	K0 V	777	4.1	30.0	7.1	14.5	0.70				
56	Gl 700.2	K0 V	530	4.4	21.8	7.0	18.9	0.84	G182-035	3353		
57	Gl 758	K0 v	522	4.6	8.4	6.4	17.6	0.95				
58	Gl 895.4	K0 V	548	4.4	-2.1	6.7	17.8	0.87	G217-011	544		LTT 16916
59	Gl 631	K0 Ve	956	4.4	28.4	5.8	10.5	0.83		3224		
60	Gl 217	K1 V	622	4.2	4.4	7.4	17.6	0.73	G096-051	1783		
61	Gl 762.1	K1 V	438	4.6	18.0	6.6	20.6	0.98	G229-033	3466		
62	Gl 778	K1 V	585	4.2	-4.2	7.3	18.2	0.76	G186-011	481		
63	Gl 211	K1 Ve	858	4.3	11.9	6.2	12.1	0.79		1774		
64	HD 40676	K2	748	3.9	11.7	7.8	16.4	0.62				
65	Gl 706	K2 v	975	4.2	24.2	6.4	11.3	0.73	G205-005	3363		
66	GJ 1240	K2 v	650	4.1	-14.1	7.6	17.5	0.69			U 469	LTT 7720
67	Gl 28	K2 Ve	650	4.2	-22.6	7.4	17.1	0.71	G132-015	1125		

Table 4
Target Stars for the 10-m "Solar-Class" Survey
 (cont'd)

	Star	Spectral Type	Sig10 (pas)	OrbIO (au.)	b" (deg.)	V	D (pc)	Mass (Mo)	Giclas	LHS	Vyss. UGPMF	Other
68	Gl 282 A	K2 Ve	878	4.0	9.1	7.2	13.5	0.65	G1 12-037		U165	Binary 58" sep.
69	Gl 329	K2/3 III	901	3.7	13.2	8.7	15.3	0.52				
70	Gl 174	K3 V	888	3.9	-16.5	8.0	14.0	0.60	G008-051			
71	Gl 183	K3 V	1193	4.2	-27.2	6.2	9.0	0.75		200	U102	
72	Gl 250 A	K3 V	1247	4.1	-2.2	6.6	9.2	0.68		1875	U148	Binary 58" sep.
73	Gl 621	K3 V	756	3.9	24.2	8.4	16.6	0.59	G153-049		U408	
74	Gl 688	K3 V	816	4.4	17.7	6.5	12.3	0.83				
75	Gl 716	K3 V	716	4.4	-4.2	6.8	14.1	0.83				
76	Gl 892	K3 V	1564	4.2	-3.2	5.6	6.8	0.76		71		
77	Gl 770	K3/4 V	648	4.6	-23.9	6.2	13.9	0.97			U479	
78	Gl 727	K4	763	4.0	5.5	8.0	15.6	0.64	G141-037		V325	
79	Gl 775	K4 V	797	4.1	-14.2	7.5	14.2	0.70				
80	Gl 782	K4 Vp	886	3.7	-26.2	8.9	15.8	0.50		3526	V330	Binary 58" sep.
81	Gl 282 B	K5	1112	3.6	9.1	8.9	13.5	0.46	G1 12-038			
82	Gl 622	K5	1235	3.2	18.7	10.4	15.1	0.33		3191		
83	Gl 171.2A	K5 ep	774	3.9	-13.4	8.4	16.4	0.59	G008-044			Binary 126" sep.
84	Gl 49	K5 V	2212	3.1	-0.5	9.6	8.9	0.30	G243-052	1179	v002	LFT 94 Wolf 46
85	Gl 69	K5 V	1029	3.7	1.5	8.4	13.3	0.52	G244-033	1291	V381	
86	Gl 204	KS V	834	4.0	-20.0	7.7	14.0	0.66	G099-012	1763	V463	
87	GJ 1094	K5 V	808	3.9	-0.6	8.4	15.8	0.58			U152	LTT 2722
88	Gl 653	K5 V	1148	3.8	20.9	7.7	11.3	0.57	G019-013	431	V787	A Wolf 635 LFT 1316
89	Gl 241	K6	668	4.0	8.6	8.1	17.5	0.66	G109-020		V478	
90	Gl 818	K6 v	715	4.0	-25.5	8.3	17.1	0.62	G025-016	3624	V831	
91	Gl 719	K6 Ve	678	4.0	23.6	8.1	17.2	0.66	G227-036			BYDRA
92	Gl 154	K7	1129	3.4	-22.1	9.6	14.5	0.40	G006-034		V104	
93	Gl 215	K7	1072	3.6	16.6	9.0	14.0	0.46	G249-018	1782	V466	
94	Gl 726	K7	1022	3.6	-0.8	8.8	14.1	0.48	G021-024		V805	
95	Gl 52	K7 V	976	3.6	1.1	9.0	14.9	0.48	G243-060	136	V365	
96	Gl 169	K7 V	1199	3.7	-18.1	8.3	11.7	0.50			V008	
97	Gl 673	K7 V	1859	3.6	20.0	7.5	7.8	0.48	G019-024	447	V794	
98	Gl 273.1	K8	446	4.6	21.4	7.7	20.7	0.94	G090-001		V880	
99	Gl 824	K8	640	4.3	-26.4	7.9	16.4	0.78			V833	
100	Gl 172	K8 Ve	1398	3.7	3.9	8.6	10.2	0.49	G1 75-042	1688	V449	

FIGURE CAPTIONS

Figure 1, These stars in NGC 2420 were observed with the Palomar 5-m telescope,

Figure 2. We show the Allan variance of the positional uncertainty of 15 stars in NGC 2420 observed with the Palomar 5-m.

Figure 3. The planet-star configuration illustrates the astrometric signal produced

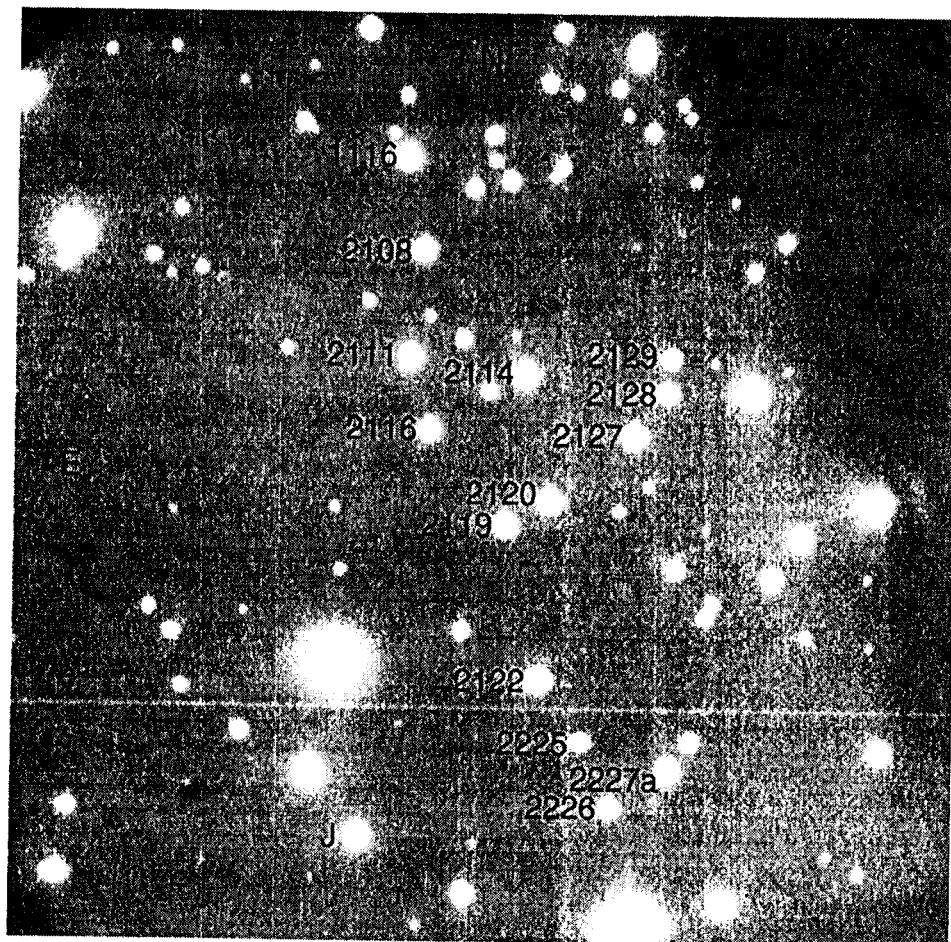
Figure 4. These are the minimum peak-to-peak amplitudes of stellar motion for 30-detections vs. the orbital period of a planet. The plot assumes 2 observation/yr for 10 yr. Each observation has a precision of 150 *pas*. For periods longer than 10 years, the curve shows the worst-case phase.

Figure 5. Distortion at the Keck telescope is well below the precision of the astrometric measurements. The solid curve is the as-designed distortion across an 84 *as* field-of-view. The other curves show how the distortion changes when the secondary mirror is misaligned.

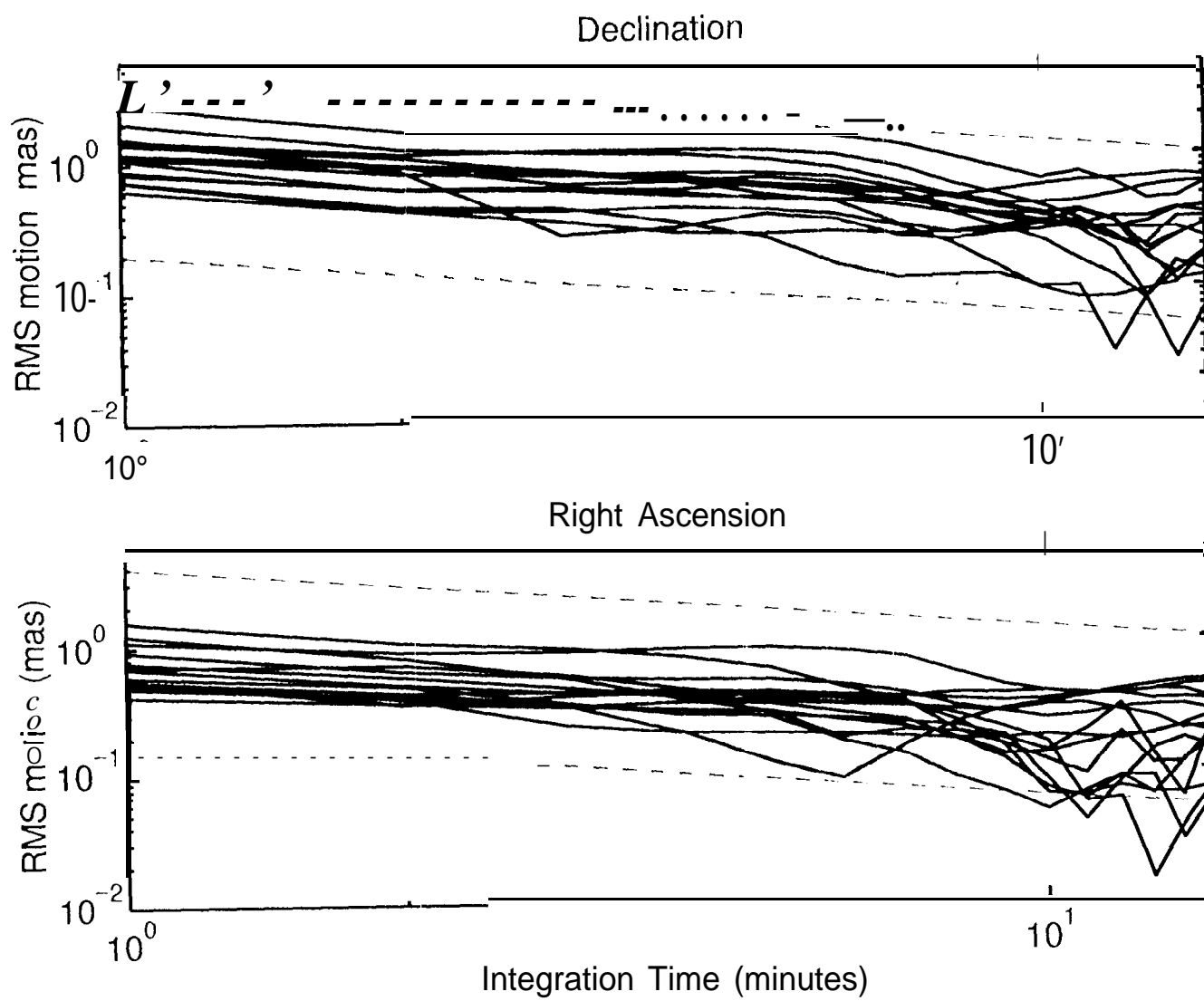
Figure 6. We show the peak-to-peak amplitudes of stellar motion for the 838 stars potentially sampled by the 10-m program assuming the presence of a Jupiter-mass planet in a 10-yr orbit. Stars are sorted by spectral type and sub-type, with each sub-type sorted by amplitude. The y-axis of the plot cuts off Barnard's star, an M5 dwarf, that would have a 14.5 *mas* amplitude.

Figure 7. We show the parameter spaces explored (shaded regions) for 3σ -detections in a 10-yr program at the 10-, 5-, and 1.5-m telescopes. 1.6 hr/yr are allocated to each source. The Keck telescope explores the 4-5 au. region for nearly all the 100 program stars. The jagged edges of the shaded regions is due to varying distances and masses of the target stars.

Figure 8. The semi-major axes parameter space searched with a 10-m telescope expands as the observational program length increases. The 10-yr search region is identical to that in Figure 7.



PRAUDO/SHAKLAN FIG 1



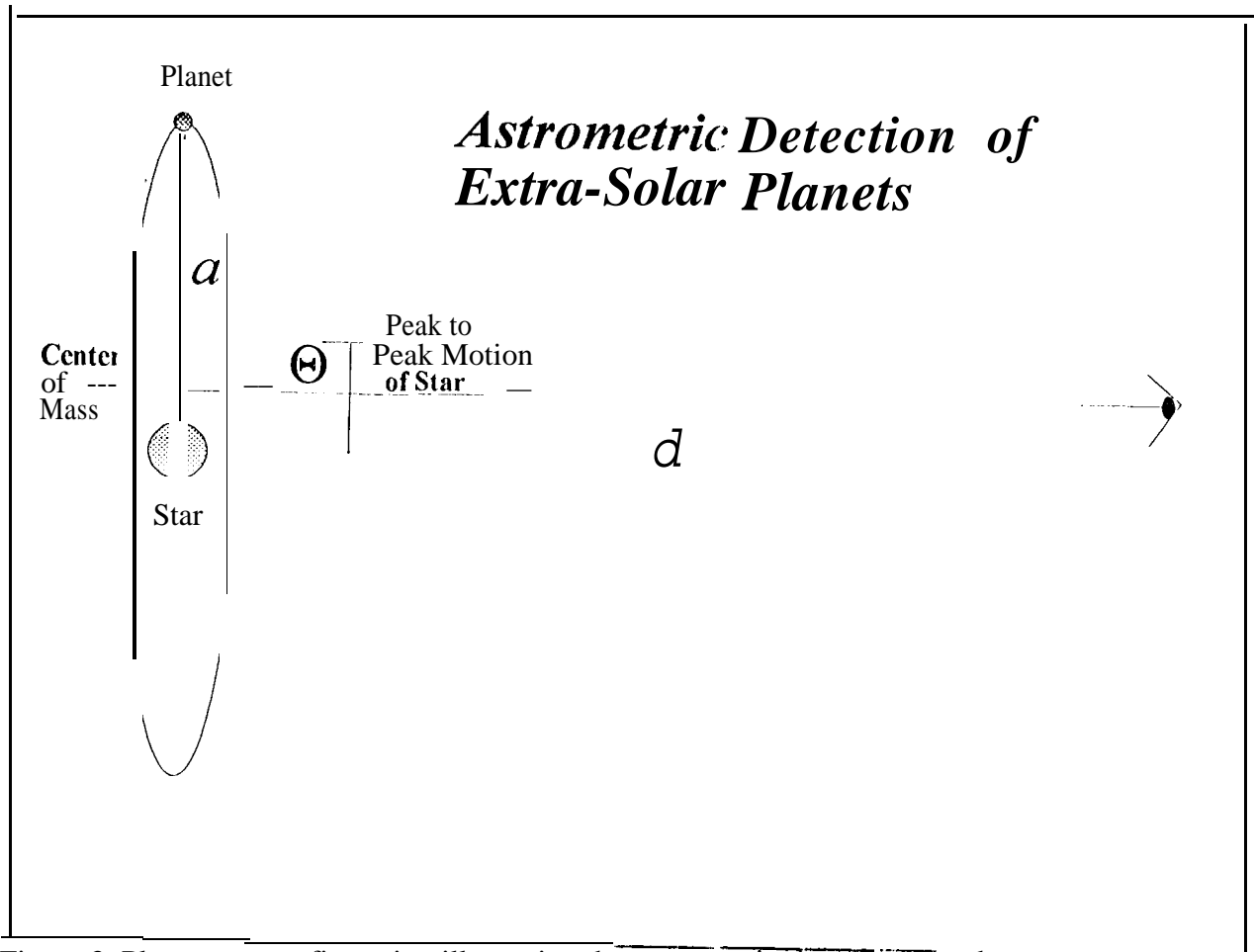
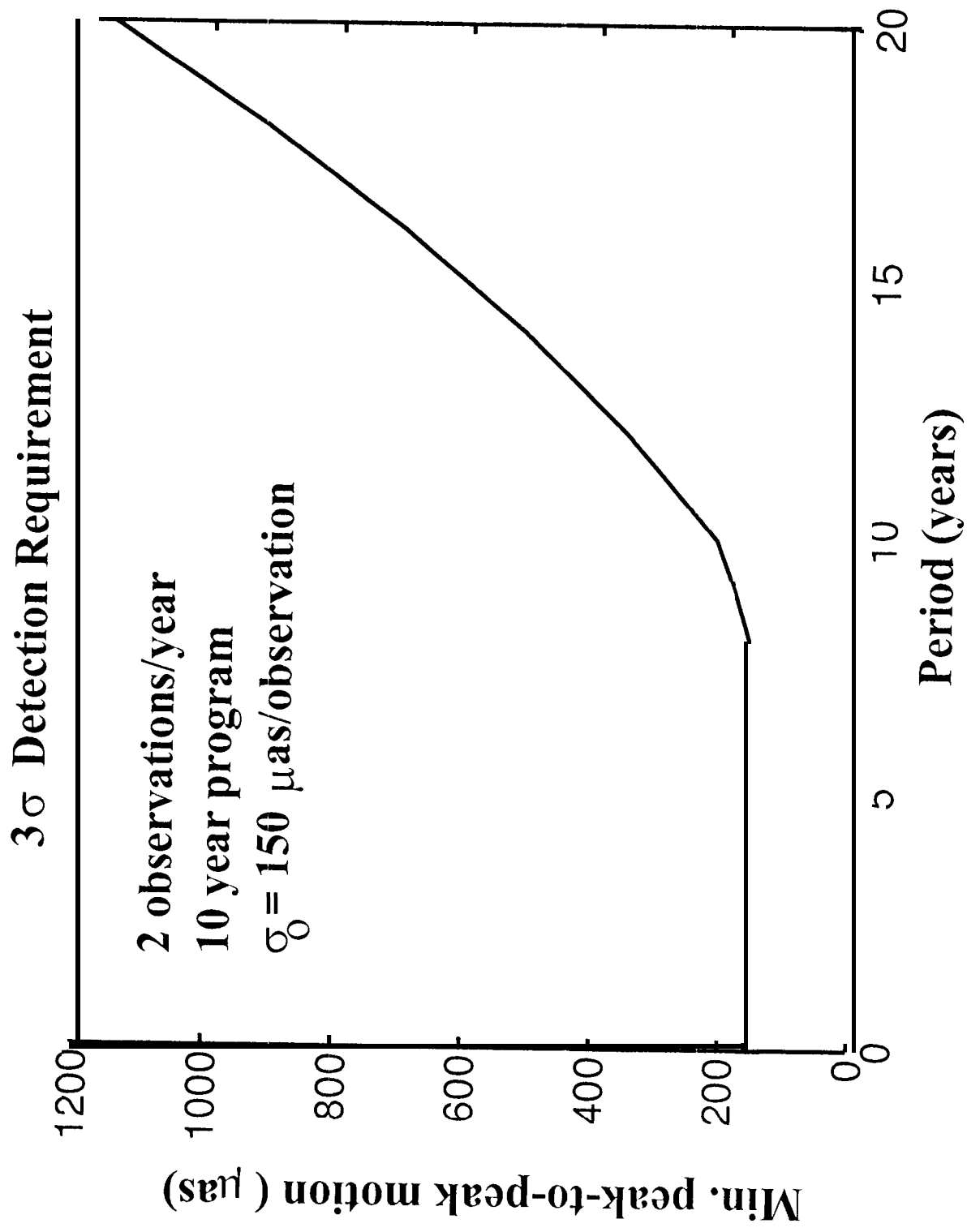
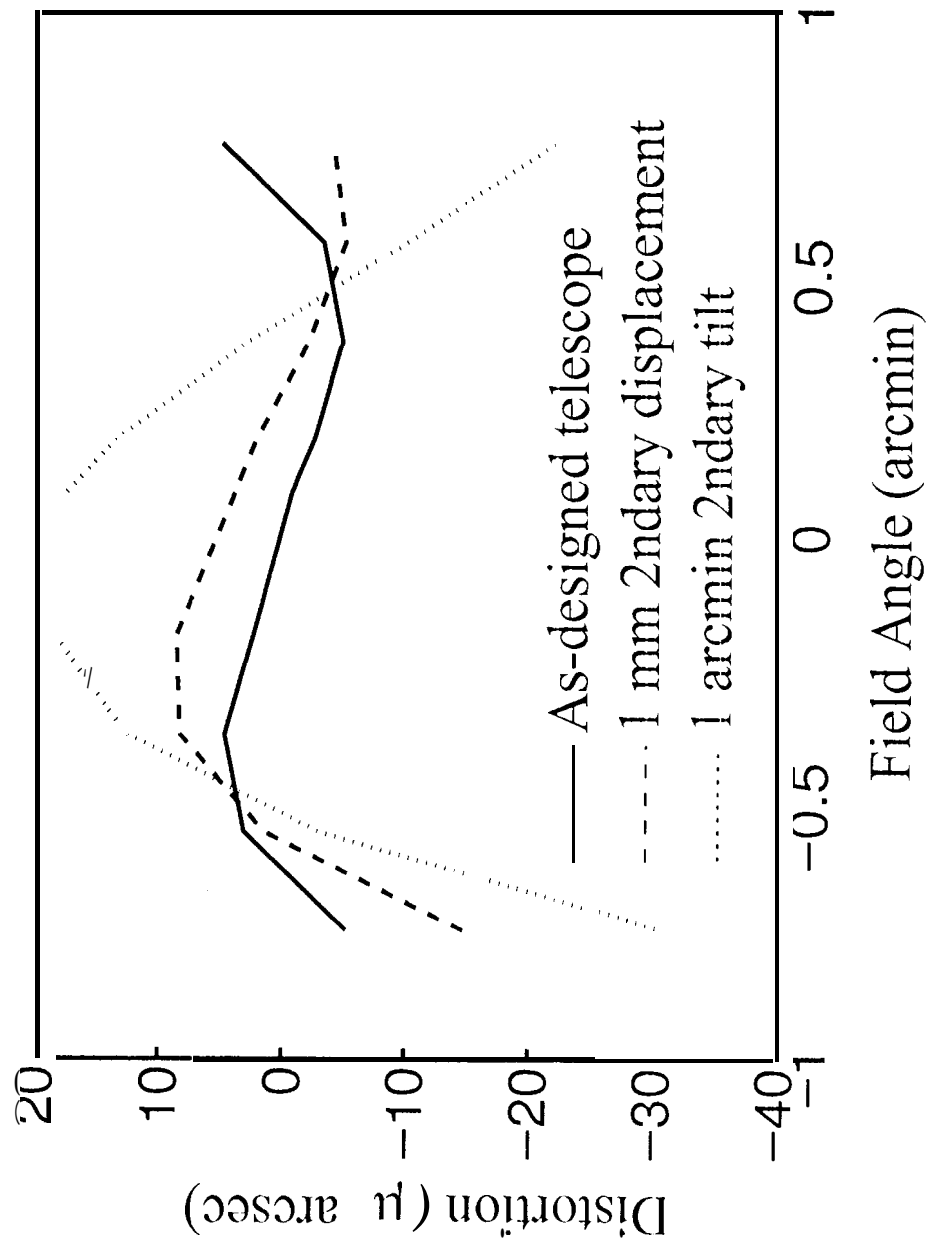
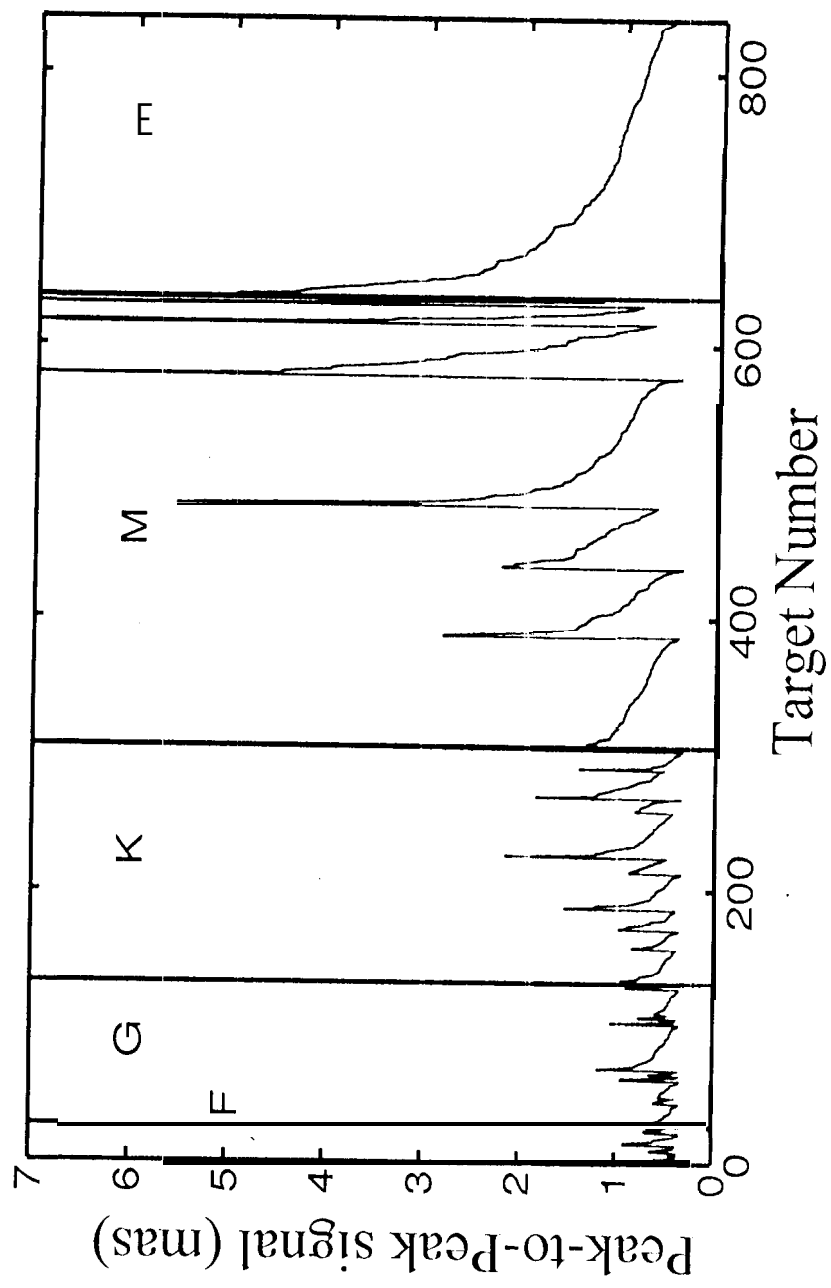
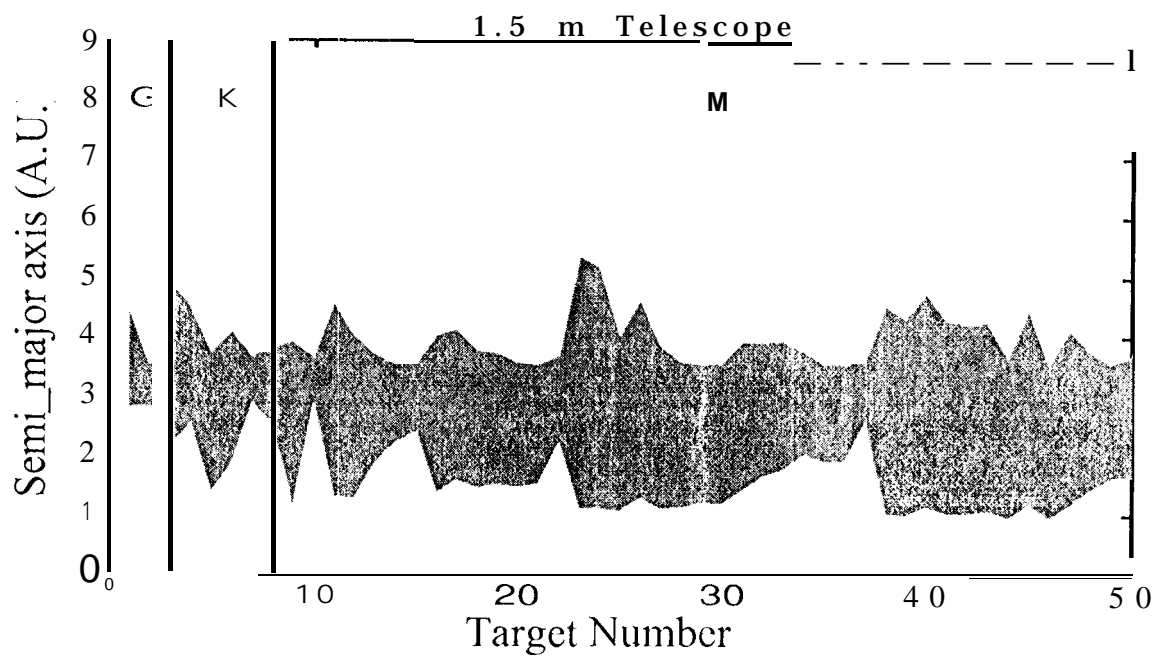
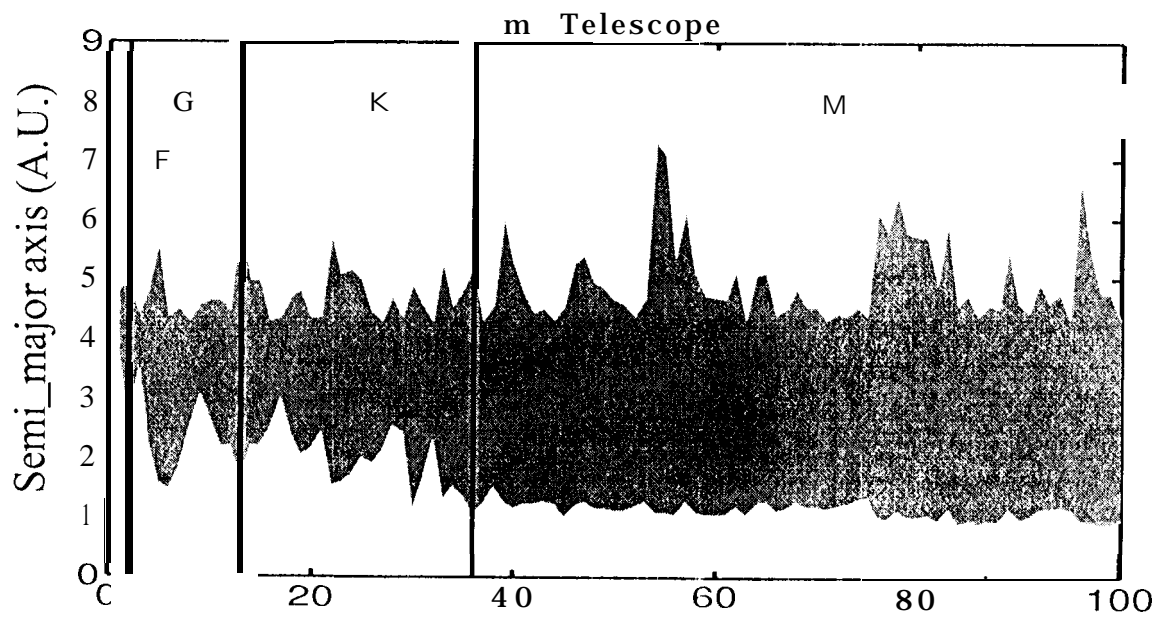
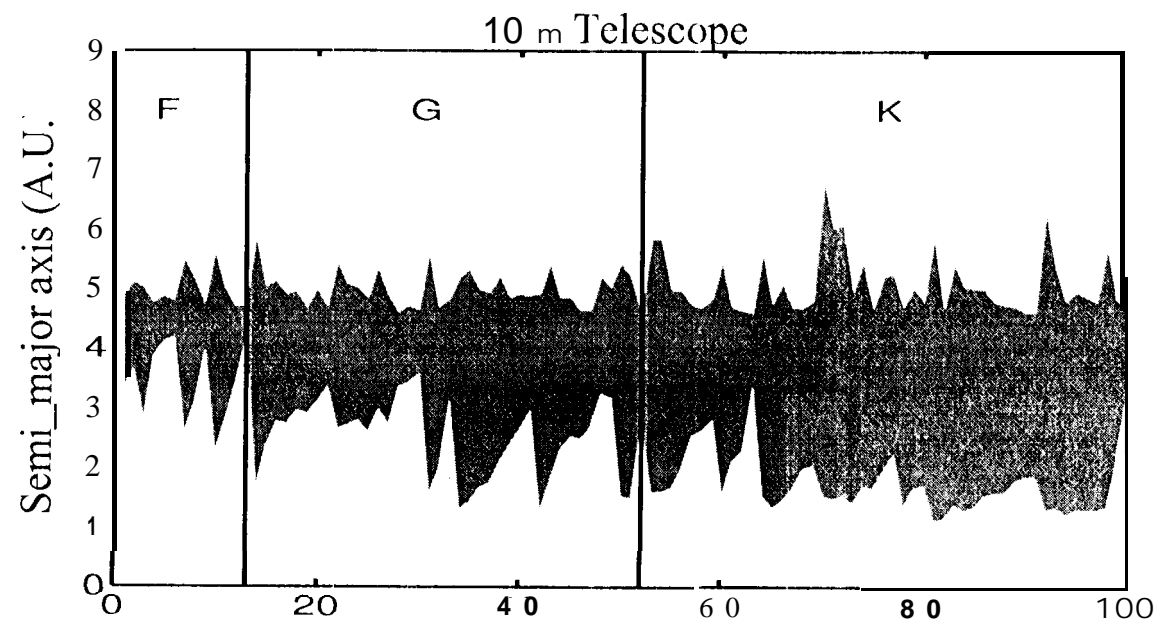


Figure 3. Planet-star configuration illustrating the astrometric signal produced.









Appendix

The target star position is measured relative to the reference frame formed by the background stars. Observations made at different epochs are registered to one another using an affine transformation that is defined with a least squares model. Simple models (e.g. linear in each axis) require fewer reference stars and are less sensitive to random noise in their parameter variance than higher-order models. Higher-order models, on the other hand, are sometimes required to account for aberrations and other systematic effects. In this appendix, we show how the reference star distribution and choice of affine transformation relate to the astrometric sensitivity of the model.

Since the target stars are generally brighter than the background stars, astrometric precision is limited by the photometric noise associated with the background stars. In this appendix, we compute the noise in the estimate of the target star position as a function of the reference frame spatial and brightness distribution, for both linear and second-order models.

The affine transformation is defined by a set of parameters, β , that provide a least squares solution to the equation

$$W^{-1}Y = W^{-1}X\beta \quad A1$$

Y is the vector of measured background star positions in frame i , which for the x axis

positions is given by

$$\begin{bmatrix} x_{i,1} \\ x_{i,2} \\ \vdots \\ x_{i,n} \end{bmatrix} \quad A2$$

where the second subscript refers to star number, and there are n background stars.

X defines the affine transformation in terms of measured positions in frame $j \neq i$. For three linear terms per axis, X is given by

$$X = \begin{bmatrix} 1 & x_{j,1} & y_{j,1} \\ 1 & x_{j,2} & y_{j,2} \\ \vdots & \vdots & \vdots \\ 1 & x_{j,n} & y_{j,n} \end{bmatrix} \quad A3$$

W^{-1} gives the weight of each equation. When the measurement error of each star is independent with a standard deviation $\sigma_m, m = 1 \dots n$, W takes the form

$$W = \begin{bmatrix} \sigma_1 & & & \\ & 0 & & \\ & & \ddots & \\ & 0 & & \\ & & & \sigma_n \end{bmatrix} \quad A4$$

The noise will be independent when, as considered below, the noise is due to the photon statistics of each star.

The solution to eq. A1 is given by (see e.g. Press *et al*, 1989)

$$\hat{\beta} = (X^T V^{-1} X)^{-1} X^T V^{-1} Y \quad A5$$

with $V = W^T W$, the diagonal matrix of positional variances. The covariance matrix of the solution is given by

$$\text{cov}(\hat{\beta}) = (X^T V^{-1} X)^{-1} \quad \text{A6}$$

We now assume that the target star is nominally located at the center of the coordinate frame. The variance of the positional error of the center of the frame is given by the first term in the covariance matrix, $\sigma_f^2 = \text{cov}(\hat{\beta})(1, 1)$. For the linear model of eq. A3, this term is

$$\sigma_f^2 = \frac{\sum \frac{x_m^2}{\sigma_m^2} \sum \frac{y_m^2}{\sigma_m^2} - \left(\sum \frac{x_m y_m}{\sigma_m^2} \right)^2}{\sum \frac{1}{\sigma_m^2} \sum \frac{x_m^2}{\sigma_m^2} \sum \frac{y_m^2}{\sigma_m^2} - \sum \frac{1}{\sigma_m^2} \sum \frac{x_m y_m}{\sigma_m^2} - \left(\sum \frac{x_m}{\sigma_m^2} \right)^2 \sum \frac{y_m^2}{\sigma_m^2} + 2 \sum \frac{x_m}{\sigma_m^2} \sum \frac{y_m}{\sigma_m^2} \sum \frac{x_m y_m}{\sigma_m^2} - \left(\sum \frac{y_m}{\sigma_m^2} \right)^2 \sum \frac{x_m^2}{\sigma_m^2}} \quad \text{A7}$$

We can rewrite this equation in terms of the moments of the background star distribution and the number of photons in the reference frame. If all stars have the same point spread function, with root-mean-squared width σ_c , and if the centroid measurement noise on star m is due strictly to the finite number of detected photons, N_m , then the positional variance of star m is given by

$$\sigma_m^2 = \frac{\sigma_c^2}{N_m} \quad \text{A8}$$

Substituting this into eq. A7, and defining the moments of the field as

$$M_{1x} = \frac{\sum N_m x_m}{\sum N_m} \quad \text{A9}$$

$$M_{2x} = \frac{\sum N_m x_m^2}{\sum N_m} \quad \text{A10}$$

$$M_{x,y} = \frac{\sum N_m x_m y_m}{\sum N_m} \quad \text{A11}$$

and similarly for M_{1y} and M_{2y} , one then finds

$$\sigma_f^2 = \frac{\sigma_c^2}{\sum N_m} \cdot \frac{M_{2x} M_{2y} - (M_{xy})^2}{M_{2x} M_{2y} - (M_{xy})^2 - M_{1x}^2 M_{2y} + 2 M_{1x} M_{1y} M_{xy} - M_{1y}^2 M_{2x}} \quad \text{A12}$$

Eq. A12 shows that the target star positional variance is given by the width of the stellar images σ_c , the total light in the frame $\sum N_m$, and a function of the first and second moments of the reference frame.

If the plate scale model was not required, and if only one reference star of brightness $\sum N_m$ was present, then the first term of eq. A 12 would be the reference frame positional variance, given by σ_1^2 . The second term containing the moments can be thought of as the inefficiency of the plate scale model. The positional variance for astrometry is then the product of the noise associated with a single reference star of brightness $\sum N_m$, and a frame efficiency factor F given by the ratio of moments in eq. A12.

For higher order transformations, the number of terms in eq. A12 grows rapidly. Matrix inversion for a full quadratic model (six terms per axis) is made possible under the assumption that the field is point symmetric. In that case, the frame variance is given by

$$F = \frac{M_{4x}M_{4y} - (M_{2(xy)}^2)}{M_{4x}M_{4y} - (M_{2(xy)}^2) - M_{2x}^2M_{4y} + 2M_{2x}M_{2y}M_{2(xy)} - M_{2y}^2M_{4x}} \quad \text{A13}$$

The presence of fourth-order moments implies that for quadratic models the frame variance is highly sensitive to the distribution of reference stars. Note that for the linear model, $F = 1$ when the field is assumed to be point symmetric.

An interesting characteristic of eq. A12 is that the variance depends on the shape but not the size of the field. This is easily shown by substituting $x' = ax$ into eqs. A9 to A11. a being a scale factor. This is in contrast to differential centroid noise due to the atmosphere, which is not considered in this appendix. Atmospheric noise, in the small field limit, increases linearly with field diameter.

The value of I' depends on the distribution of reference stars. We have arrived at a mean value of I' by performing a Monte-Carlo simulation of reference frames. In the simulation, reference stars having $V \leq 21$ were chosen with a magnitude distribution taken from Allen (1973), and randomly positioned within the field-of-view of the 10-m telescope (84 arcsec, Table 3). Reference frames were required to have at least 6 stars and were defined over the whole sky. The moments were evaluated according to eqs. A9 to A11 and I' was evaluated according to eq. A12. The result was that the mean value of I' for the linear affine transformation was $I' \approx 5$.

Thus, as reported in §7.1, the reference frame, when reduced using a linear affine transformation, is effectively five times fainter than the summed light of the reference frame. The same fields reduced with a full quadratic model had an effective brightness 31 times fainter than the summed reference frame.